

1 **Comparisons of predicted bore evolutions by the**
2 **Benjamin-Davis-Ono and Navier-Stokes equations for**
3 **idealized mesopause thermal ducts**

4
5 B. Laughman, D. C. Fritts, and J. Werne

6 NorthWest Research Associates, CoRA Division, Boulder, Colorado

7 Correspondence to: B. Laughman (laughman@cora.nwra.com)

8
9 **Abstract**

10 Numerical simulations are performed employing two numerical models to contrast
11 nonlinear bore evolutions predicted by the Benjamin-Davis-Ono (BDO) equation with
12 evolutions described by the Navier-Stokes (NS) equations. The first model is a simple
13 one-dimensional (1D) solver of the BDO equation; the second describes the nonlinear
14 two-dimensional (2D) dynamics of the NS equations. Both utilize the Boussinesq
15 approximation. Due to their simpler, horizontally-isotropic nature, only isolated thermal
16 ducts are considered in this study. Simulations assume an initial long-wave perturbation
17 and address the influences of perturbation amplitude and wavelength, viscosity, and non-
18 zero background stability on the resulting evolutions. Results indicate that the BDO
19 equation provides reasonable predictions of bore character and evolution for conditions
20 that satisfy its underlying assumptions. BDO predictions fail to describe bore character
21 and evolution in cases where either the initial perturbations or the thermal environment
22 differ significantly from BDO assumptions. Predictions employing the NS equations will

23 thus provide more realistic guidance in the interpretation and understanding of bores
24 observed in the mesopause region for general environments.

25

26 **1 Introduction**

27 For the past decade there has been a continuing effort to explain mesospheric bore
28 observations. These efforts began when Dewan and Picard (1998) applied hydraulic
29 theory to apparent observations of bores in the mesosphere and lower thermosphere
30 (MLT), providing a qualitative starting point for understanding these phenomena. Dewan
31 and Picard (2001) furthered these efforts by examining potential forcing mechanisms
32 with scales relevant to MLT bore observations. Subsequent numerical studies performed
33 by Seyler (2005) and Laughman et al. (2009b) demonstrated the viability of numerical
34 models employing the Navier-Stokes (NS) equations to generate bore-like evolutions
35 from initial long-wave perturbations.

36 The general study of solitons and bores in fluids has a much longer history, dating
37 back to work done by Airy (1845), Lord Rayleigh (1908) and Lamb (1932). The KdV
38 equation was the first clear and concise description of the balance between nonlinear
39 steeping and dispersion which supports the existence of solitons, waves of permanent
40 form (Korteweg and de Vries, 1895). While this theory is an excellent approximation for
41 surface waves, it is less applicable to fluids with continuous density gradients. Internal
42 solitary waves are better described by the Benjamin-Davis-Ono (BDO) equation and
43 indeed this equation has provided guidance in studies of tropospheric bores such as the
44 Morning Glory in Australia (Christie, 1989; Porter and Smyth, 2001).

45 The goal of this paper is not to engage in an in-depth exposition of the KdV
46 equation, the BDO equation, or their relative similarities and differences, though we will
47 touch on a few points of each. A wealth of literature already exists detailing the
48 characteristics of each, including, but not limited to, Ono (1975), Koop and Butler
49 (1981), Grimshaw (1980), Christie (1989), and others (Hammack and Segur, 1974) which
50 we reference in Section 2.

51 Rather, the goal of this work is to address the conditions under which the BDO
52 equation offers a good approximation to solutions of the NS equations in idealized
53 environments and to explore the differences that arise when less idealized environments
54 are considered, specifically a non-zero background stability and the effects of viscosity.
55 It should be noted that the BDO equation has been extended to include viscous effects,
56 compressibility effects, and radiative effects due to more complicated environments than
57 those first considered by Benjamin (1967) (e.g. Grimshaw, 1980; Maslowe and
58 Redekopp, 1980)). Our comparison studies make use of only the simple BDO equation
59 and our study of non-idealized environments is confined to use of our 2D NS model.

60 We discuss the KdV and BDO equations in Section 2. Section 3 describes the
61 numerical BDO and NS models used for these studies, including our non-
62 dimensionalization. Section 4 presents and contrasts the results of our BDO solutions
63 with those of the NS equation for a variety of initial long-wave length scales and
64 amplitudes. Also presented are results of our NS model assuming finite viscosity and
65 non-zero background stabilities. A discussion of our results and our conclusions are
66 provided in Section 5. Appendix A contains additional details about the BDO theory
67 presented in Section 2.2.

68 **2 The KdV and BDO equations**

69 While the focus of this study is the comparison of bore evolutions predicted by
70 the BDO and NS equations for varying initial conditions and environments, it is useful to
71 first discuss the KdV equation. KdV theory is qualitatively similar to BDO theory and
72 consists of a simpler formulation.

73 **2.1 The Korteweg-de Vries equation (KdV)**

74 The KdV equation is a finite amplitude “fairly long” (i.e. weakly dispersive) wave
75 approximation for surface wave motion in a 2D channel flow. The fluid density is
76 assumed to be constant while the density of the overriding fluid (typically air) is assumed
77 to be zero. Typical flow parameters include the undisturbed fluid depth, H , and the
78 perturbation of the free surface from its undisturbed level, $\eta(x,t)$. Because the
79 wavelengths considered are fairly long the dispersion relation is not constant and takes
80 the form

81

$$82 \quad c = c_0(1 - \beta k^2) \quad (1)$$

83

84 For surface water waves, the long-wave phase speed is $c_0 = (gH)^{1/2}$ and $\beta = 1/6 H^2$
85 (Benjamin, 1967; Miles, 1981) and the wavenumber is $k = 2\pi/\lambda$. The dimensional form
86 of the KdV equation is then (Hammack and Segur, 1974)

87

$$88 \quad \frac{\partial \eta}{\partial t} + c_0 \frac{\partial \eta}{\partial x} + \frac{3}{2} \frac{c_0}{H} \eta \frac{\partial \eta}{\partial x} + \frac{1}{6} c_0 H^2 \frac{\partial^3 \eta}{\partial x^3} = 0 \quad (2)$$

89

90 The coefficient of the nonlinear term is $3/2 c_0/H$ and the coefficient of the linear
 91 dispersion term is $1/6 c_0 H^2$. The competing effects of nonlinearity and dispersion are
 92 central to KdV and BDO theory.

93 The KdV equation has stationary solutions, waves of permanent form, which
 94 represent a balance of dispersive and nonlinear effects. These solutions include periodic
 95 cnoidal waves (which we do not consider) and solitons of the form

$$96 \quad \eta(x,t) = \eta_0 \operatorname{sech}^2 \left\{ (x - c_b t) \sqrt{\frac{3\eta_0}{4H^3}} \right\} \quad (3)$$

98
 99 where the KdV soliton velocity, c_b , is greater than the long wave phase speed, c_0 , and is
 100 given by

$$101 \quad c_b = c_0(1 + \eta_0 / 2H) \quad (4)$$

102
 103
 104 For the KdV equation, the balance between nonlinear steepening (proportional to
 105 η_0/H) and linear dispersion (proportional to H^2/λ^2 as seen in the dispersion relation) can
 106 be quantified by the parameter $a\lambda^2/H^3$. Following Lighthill's treatment (1978), if one
 107 regards the amplitude of a soliton to be half its height, $a = 1/2\eta_0$, and its "wavelength" to
 108 be the range over which the height is greater than some percentage of its maximum value,
 109 say 3%,

$$110 \quad \lambda = 2[\operatorname{ArcSech}(\sqrt{0.03})] \sqrt{\frac{4H^3}{3\eta_0}}, \quad (5)$$

112

113 then we obtain a value of $a\lambda^2/H^3 = 16.14 \sim 16$. It is noteworthy that for solitons of any
114 geometry this parameter's value is independent of H , λ , and η_0 . If one wishes to instead
115 regard the "wavelength" to be only the square root term in Eq. 5 and the amplitude to
116 simply be $a = \eta_0$ then $a\lambda^2/H^3 = 1.333 \sim 1$, indicating the relatively equal strengths of
117 dispersive and steepening effects. For the remainder of this paper we will denote
118 amplitude as η_0 .

119 Finally, it should be noted that due to the way it is derived, any initial perturbation
120 that evolves according to the KdV equation will propagate preferentially in one direction,
121 with the nonlinear evolution proceeding one direction and a possible dispersive
122 component proceeding in the other in a frame moving with speed c_0 . (Benjamin, 1967)

123 2.2 The Benjamin-Davis-Ono (BDO) equation

124 The development of the BDO equation is qualitatively similar to that of the KdV
125 equation. Fairly long waves of small but finite amplitude are considered and the result is
126 an equation which contains competing dispersion and nonlinear steepening terms, and
127 which has a soliton solution. However, whereas the KdV equation was derived for
128 surface waves and evolves the surface displacement $\eta(x,t)$, the BDO equation is valid for
129 internal waves present in a deep, density stratified fluid and evolves the displacement of
130 the fluid throughout its vertical extent, which we denote $\eta(x,z,t)$. Examples of density
131 profiles first considered in the development of BDO theory are described by Eq. A.3 and
132 depicted in Figure 1 (Benjamin, 1967; Davis and Acrivos, 1967). Panel (a) shows the
133 density profile applicable to mesospheric bore modeling while panel (b) shows the profile
134 similar to what we actually model. Under assumptions of vertical anti-symmetry and the

135 Boussinesq approximation, the two profiles have the same dynamics. In both, the length
 136 h is defined as the vertical range over which the density is variable. ρ_1 and ρ_2 are
 137 arbitrary constant densities and the mean density, $\bar{\rho}_0$, is equal to the density at $z = 0$,
 138 again due to anti-symmetry.

139 Associated with each density profile is a corresponding stability profile,

140

$$141 \quad N^2(z) = \frac{g}{\bar{\theta}_0} \frac{d\theta_0(z)}{dz} = -\frac{g}{\bar{\rho}_0} \frac{d\rho_0(z)}{dz} \quad (6)$$

142

143 where N^2 is the buoyancy frequency squared, g is acceleration due to gravity, $\rho_0(z)$ is the
 144 unperturbed density profile, $\theta_0(z)$ is the unperturbed potential temperature profile, and
 145 $\bar{\rho}_0$ and $\bar{\theta}_0$ are the mean values of the density and potential temperature profiles. The
 146 equivalence of $\theta_0(z)$ and $\rho_0(z)$ defined by Eq. 6, as well as the use of $\bar{\theta}_0$ and $\bar{\rho}_0$ in place
 147 of $\theta_0(z)$ and $\rho_0(z)$ is valid under the Boussinesq approximation where variations of $\theta_0(z)$
 148 and $\rho_0(z)$ about their mean values are small. It should be noted that mesospheric bore
 149 dynamics can be on the order of a scale height, and consequently the results reported in
 150 this paper must be applied to observation with caution. The comparison of the BDO
 151 model with the NS results is unaffected, however, as both make the Boussinesq
 152 approximation. Panel (c) shows a stability profile which corresponds to the density
 153 profile in panel (a), though with the length scale doubled in order to make use of profile
 154 (b), vertical anti-symmetry about $z = 0$, and the Boussinesq approximation for our
 155 comparison studies. Panel (d) displays the modal function, $\phi(z)$, associated with the
 156 $N^2(z)$ profile in panel (c) and will be discussed further below.

157 The displacement, $\eta(x,z,t)$, can be separated into two functions, a horizontally
 158 dependant function that evolves in time, and a time independent modal function that
 159 varies with the vertical coordinate (Ono, 1975; Christie, 1989),

160

$$161 \quad \eta(x, z, t) = A(x, t) \phi(z) \quad (7)$$

162

163 The modal function, $\phi(z)$, and the long wave phase speed, c_0 , both depend on the
 164 specific form of $N^2(z)$ being considered (see Appendix A for details). The dispersion
 165 relation for “fairly long” internal waves is

166

$$167 \quad c = c_0(1 - \gamma|k|) \quad (8)$$

168

169 where γ is a constant that depends on the specific density profile being considered. This
 170 contrasts with the dispersion relationship for surface waves (Eq. 1) and unsurprisingly
 171 yields an evolution equation with a different dispersion term than the KdV equation,

172

$$173 \quad \frac{\partial A}{\partial t} + c_0 \frac{\partial A}{\partial x} + \alpha A \frac{\partial A}{\partial x} + \delta \frac{\partial^2}{\partial x^2} \mathcal{H}(A) = 0 \quad (9)$$

174

175 Here, $\mathcal{H}(A)$ is the Hilbert transform of A , c_0 is the long wave phase speed, and the
 176 coefficients of the nonlinear term, α , and the dispersion term, δ , are functions of c_0 and
 177 $\phi(z)$ (see Appendix A for further details).

178 Stationary solutions of the BDO equation are solitons. However, unlike the
 179 soliton solutions of the KdV equation, the solitons of the BDO equation are algebraic in
 180 nature, taking on the form

181

$$182 \quad A(x,t) = \frac{\eta_0 \lambda^2}{(x - c_b t)^2 + \lambda^2} \quad (10)$$

183

184 By inspection, λ is the half width at half maximum (HWHM) of the BDO soliton. The
 185 velocity is given by

186

$$187 \quad c_b = c_0 + \frac{1}{4} \eta_0 \alpha = c_0 + \frac{\delta}{\lambda} \quad (11)$$

188

189 and demonstrates the same qualitative relationship between soliton velocity, soliton
 190 height, and soliton width as the KdV soliton: as the soliton width shrinks its amplitude
 191 and velocity both increase. Also, as with the KdV soliton, the BDO soliton has a speed
 192 greater than the linear long wave phase speed c_0 .

193 The difference in the dispersion characteristics between the BDO and KdV
 194 equations also implies a different nondimensional parameter governing the relative
 195 strengths of dispersion and nonlinearity; in the case of the BDO equation the parameter is
 196 not $\eta_0 \lambda^2 / H^3$, where H is the depth of the fluid, but rather $\eta_0 \lambda / h^2$, where h is the interface
 197 thickness defined above and in Figure 1. To illustrate this difference consider a sech^2
 198 stability profile, $N^2(z) = N_0^2 \text{sech}^2(z/h)$, for which the value of $\eta_0 \lambda / h^2$ is found to be 2.5.
 199 As with the KdV soliton, this parameter is independent of η_0 , h , and λ for an arbitrary
 200 soliton and is of order ~ 1 . By contrast, computing the KdV parameter as $\eta_0 \lambda^2 / h^3$ for the

201 BDO soliton results in a function of λ/h , which contradicts the notion that solitons of *any*
 202 geometry represent the balance between nonlinearity and dispersion. Furthermore, the
 203 KdV value of 1.333 for a soliton would be obtained with $\lambda/h = 0.5333$ while the BDO
 204 value of 2.5 would require $\lambda/h = 1.0$, both of which clearly violate the assumptions of
 205 both theories that $\lambda > h$.

206 An important point to consider is that while the parameter $\eta_0\lambda/h^2$ is constant for
 207 arbitrary geometries of BDO solitons, it is a function of the density profile. By
 208 inspection of Eq. 11 $\eta_0\lambda=4\delta/\alpha$, implying that different ducting structures with different
 209 values of δ and α support different relative strengths of linear dispersion and nonlinear
 210 steepening behavior.

211 **3 Numerical models**

212 Two numerical models are employed in this study. The first is a NS model
 213 described in Section 3.1; the second is a BDO model described in Section 3.2. Both
 214 make use of the time stepping formulation and FFT routines described in Section 3.1. In
 215 order to directly compare the results of each model, both use the same raised cosine
 216 stability profile depicted in Figure 1 (panel c) and defined by Eq. 12, and both models are
 217 non-dimensionalized by the full width at half maximum (FWHM) of h and peak stability
 218 N_0^2 .

219

$$220 \quad N^2(z) = \begin{cases} N_0^2\left(\frac{1}{2}\right)[1 + \cos(\pi z/h)], & |z| \leq h \\ 0, & |z| > h \end{cases} \quad (12)$$

221

222 The cosine duct has the particular advantage that the relevant length scale for the BDO
 223 model, h in Figure 1 panel (b), and the chosen length scale for our NS model, the
 224 FWHM, is the same.

225 3.1 Navier-Stokes solver

226 Our NS studies employ a numerical code solving the incompressible Boussinesq
 227 Navier-Stokes equations for direct numerical simulations (DNS) of bore generation and
 228 morphology assumed to occur in two spatial dimensions. Previous applications of this
 229 code have described 2D bore studies (Laughman et al, 2009b) and three-dimensional
 230 (3D) studies of nonlinear dynamics, turbulence transitions, and turbulence evolutions and
 231 statistics for both stratified shear flow (Kelvin-Helmholtz) instability, or KHI, and gravity
 232 wave breaking (see Werne and Fritts, 1999, 2001; Fritts et al., 2003, 2006, 2009a,b). The
 233 code employs a pseudo-spectral solver that computes the nonlinear advection terms in
 234 physical space. Linear terms and derivatives are handled in Fourier space, and
 235 transformations between physical and Fourier space are performed by high-radix FFTs.
 236 Incompressibility (Eq. 14c) is enforced via a two-streamfunction formulation expressed
 237 as

238

$$239 \quad \vec{u} = \vec{\nabla} \times \vec{\psi} + \vec{\nabla} \times \vec{\nabla} \times \vec{\phi} + \vec{U}_0 \quad (13)$$

240

241 where the streamfunctions $\vec{\psi} = (0, 0, \psi(x, y, z))$ and $\vec{\phi} = (0, 0, \phi(x, y, z))$ are defined by
 242 the vertical velocity and the vertical vorticity fields and $\vec{U}_0 = (U_0, V_0, 0)$ is the mean
 243 horizontal velocity (Fritts et al., 2009a). Potential temperature and the two
 244 streamfunctions are advanced in time with a 3rd-order Runge-Kutta (RK) scheme (Spalart

245 et al., 1991). The velocity and vorticity fields are computed from these quantities after
 246 each RK time sub-step according to Eq. 13. The time-step is allowed to vary
 247 dynamically according to a Courant-Friedrichs-Lewy (CFL) condition of 0.68.

248 The equations being solved are the incompressible Navier-Stokes equations
 249 subject to the Boussinesq approximation

250

$$251 \quad \partial_t \vec{u} + (\vec{u} \cdot \vec{\nabla}) \vec{u} = \nu \nabla^2 \vec{u} - \vec{\nabla}(P/\bar{\rho}_0) + (\rho/\bar{\rho}_0) \vec{g} \quad (14a)$$

$$252 \quad \partial_t \theta + (\vec{u} \cdot \vec{\nabla}) \theta = \kappa \nabla^2 \theta \quad (14b)$$

$$253 \quad \vec{\nabla} \cdot \vec{u} = 0 \quad (14c)$$

$$254 \quad \rho = \bar{\rho}_0 [1 - \alpha(\theta - \bar{\theta}_0)] \quad (14d)$$

255

256 where $\theta - \bar{\theta}_0$ is small. Eq. 14 supports waves governed by the 2D dispersion relation,

257

$$258 \quad m^2 = \frac{N^2}{(U_0 - c)^2} - \frac{\partial^2 U_0 / \partial z^2}{(U_0 - c)} - k^2 \quad (15)$$

259

260 Here $\mathbf{u} = (U_0 + u, V_0 + v, w)$ is the full 3D velocity field, P is the pressure field, ρ is the
 261 density, θ is the potential temperature, and g is gravity. For the results presented in this
 262 paper U_0 is always 0, as are v and V_0 . N^2 is the buoyancy frequency defined by Eq. 6, k
 263 $= 2\pi/\lambda_x$ and $m = 2\pi/\lambda_z$, λ_x and λ_z are horizontal and vertical wavelengths, and ν and κ
 264 are kinematic viscosity and thermal diffusivity, and α is related to the coefficient of
 265 thermal expansion and is equal to $1/\bar{\theta}_0$.

266 The length scale by which we non-dimensionalize is chosen to be the FWHM of
267 our stability duct, and our time scale is chosen to be $1/N_0$, where the peak stability is
268 given by $N_0 = (|g|\alpha\beta)^{1/2}$, where β is the magnitude of the maximum value of the vertical
269 derivative of the potential temperature profile. These length and time scales define the
270 velocity scale as $u_0 = N_0 h$. The Richardson number is then $Ri = N_0^2 h^2 / u_0^2 = 1$. We set ν
271 $= \kappa$, resulting in a Prandtl number $Pr = 1$, and so both the Reynolds and Peclet numbers
272 are defined as $Pe = Re = N_0 h^2 / \nu$. According to Eq. 6 which employs the Boussinesq
273 approximation, potential temperature is proportional to the vertical integral of the N^2
274 profile and scales according to $N_0^2 h$. Units of temperature are recovered though the
275 constants g and α , which for environments appropriate to the mesopause have values of
276 9.55 ms^{-2} and $1/(8500 \text{ K})$, respectively. With a chosen length scale of 5 km and a
277 stability maximum $N_0 = 0.0523599 \text{ s}^{-1}$, our time scale is $\sim 19 \text{ s}$ and our velocity scale is
278 $\sim 262 \text{ ms}^{-1}$. We select a Reynolds number of 13090.0, corresponding to a kinematic
279 viscosity of $100 \text{ m}^2 \text{ s}^{-1}$. For effectively inviscid runs viscosity is set to the vanishingly
280 small value of $10^{-4} \text{ m}^2 \text{ s}^{-1}$ resulting in a Reynolds number of 1.309×10^{10} ; this value was
281 chosen because preliminary simulations performed with larger Reynolds numbers were
282 not noticeably different from the 10^{10} case. For all the effectively inviscid runs there is a
283 limit on how long the simulation can run until the growing undamped Gibbs noise attains
284 an amplitude comparable to the modeled dynamics (Laughman, 2009a).

285 All NS simulations presented in this paper assumed 2D nonlinear dynamics and a
286 domain having periodic horizontal boundary conditions and reflective upper and lower
287 boundaries. Unless otherwise noted, all simulations also employ 1000 spectral modes in

288 the horizontal and 2501 modes in the vertical. Specific horizontal domain sizes, x_{max} ,
 289 vertical domain sizes, z_{max} , and numbers of grid points are given in Section 4.

290 Initializing the NS model consists of defining the mean environment and the
 291 perturbation to that environment. In every run the mean wind is set to zero while the
 292 non-dimensional mean potential temperature profile in the region $|z| < 1$ is given by Eq.
 293 16a. Eq. 16b is the corresponding stability profile.

294

$$295 \quad \bar{\theta}(z) = N_B^2 z + \frac{1}{2}(1 - N_B^2) \left[z + \frac{1}{\pi} \sin(\pi z) \right] \quad (16a)$$

$$296 \quad N^2(z) = N_B^2 + \frac{1}{2}(1 - N_B^2) [1 + \cos(\pi z)] \quad (16b)$$

297

298 N_B^2 is the constant, non-dimensional background stability in the region $|z| > 1$ and is set
 299 to zero for all comparison runs with the BDO equation. For the purposes of this paper,
 300 the terms “background” or “background stability” refer to this region away from the duct
 301 with $|z| > 1$. We note that our mean temperature and stability are continuous functions
 302 while the 3rd derivative of temperature is discontinuous at $z = \pm 1$. This reduces the order
 303 of our solver to two.

304 We initialize our NS runs based on the predictions of the BDO equation for two
 305 types of perturbations, a soliton and a sinusoid. Our initialization is computed according
 306 to Eq. A.1 in the inner region and Eq. A.9 in the outer region. The vertical velocity is
 307 initialized as the partial time derivative of the fluid displacement. The temperature
 308 perturbation is computed numerically by applying $\eta(x,z)$ to the temperature field,
 309 mapping $T(x,z,t)$ to $T(x,z+\eta,t)$. Specifically, the value of the initial potential temperature
 310 at $T(x, z+\eta(x, z, 0), 0)$ is set equal to the value of the undisturbed potential temperature

311 profile, $T(z)$. For values of η where $z+\eta$ does not lie directly on a grid point a linear
 312 interpolation between neighboring grid points is used to compute $T(x,z+\eta,0)$. The initial
 313 horizontal velocity is computed numerically from the specified vertical velocity
 314 according to Eq. 13.

315 The specific forms of the soliton and soliton-like initializations are,

316

$$317 \quad \eta(x, z) = \begin{cases} S \frac{\eta_0 \lambda^2}{x^2 + \lambda^2} \phi(z), & |z| < 1 \\ 318 \quad S \frac{\eta_0 (\lambda + z - 1)^2}{x^2 + (\lambda + z - 1)^2} env(z), & z > 1 \\ 319 \quad -S \frac{\eta_0 (\lambda - z - 1)^2}{x^2 + (\lambda - z - 1)^2} env(z), & z < 1 \end{cases} \quad (17a)$$

320

$$321 \quad w(x, z) = \begin{cases} S 2c_b x \frac{\eta_0 \lambda^2}{[x^2 + \lambda^2]^2} \phi(z), & |z| < 1 \\ 322 \quad S 2c_b x \frac{\eta_0 (\lambda + z - 1)^2}{[x^2 + (\lambda + z - 1)^2]^2} env(z), & z > 1 \\ 323 \quad -S 2c_b x \frac{\eta_0 (\lambda - z - 1)^2}{[x^2 + (\lambda - z - 1)^2]^2} env(z), & z < 1 \end{cases} \quad (17b)$$

324

$$325 \quad env(z) = \frac{1}{2} \left[\tanh\left(z + \frac{z_{max}}{4}\right) - \tanh\left(z - \frac{z_{max}}{4}\right) \right] \quad (18)$$

326

327 where S modifies the amplitude of the perturbation. $S = 1$ is the soliton case while $S \neq 1$

328 defines the soliton-like cases. The sine wave initialization is given by

329

$$330 \quad \eta(x, z) = \begin{cases} \eta_0 \sin\left(\frac{2\pi}{\lambda_x} x\right) \phi(z), & |z| < 1 \\ 331 \quad \eta_0 \sin\left(\frac{2\pi}{\lambda_x} x\right) \exp\left\{\frac{-2\pi}{\lambda_x} |z - 1|\right\} env(z), & z > 1 \\ 332 \quad -\eta_0 \sin\left(\frac{2\pi}{\lambda_x} x\right) \exp\left\{\frac{-2\pi}{\lambda_x} |-z - 1|\right\} env(z), & z < 1 \end{cases} \quad (19a)$$

333

$$w(x, z) = \begin{cases} -\frac{2\pi}{\lambda_x} \eta_0 c_0 \cos\left(\frac{2\pi}{\lambda_x} x\right) \phi(z), & |z| < 1 \\ -\frac{2\pi}{\lambda_x} c_0 \eta_0 \cos\left(\frac{2\pi}{\lambda_x} x\right) \exp\left\{\frac{-2\pi}{\lambda_x} |z-1|\right\} env(z), & z > 1 \\ \frac{2\pi}{\lambda_x} c_0 \eta_0 \cos\left(\frac{2\pi}{\lambda_x} x\right) \exp\left\{\frac{-2\pi}{\lambda_x} |-z-1|\right\} env(z), & z < -1 \end{cases} \quad (19b)$$

337

338 Since there is no relationship between λ and η_0 for a sine wave, the variable S serves no
 339 purpose here; a value of S other than 1 is absorbed by the amplitude η_0 . The purpose of
 340 the envelope function defined by Eq. 18 is to force the vertical velocity perturbation to a
 341 value of strictly zero at the upper and lower boundaries. The reason for this is that the
 342 spectral formulation of the code requires a vertical velocity of zero at these boundaries;
 343 failing to do so results in significant Gibbs oscillation. A number of simulations were
 344 performed to test the effect of this envelope on the resulting evolution, and the resulting
 345 choice of vertical domain size minimizes these effects without unduly sacrificing
 346 efficiency.

347 3.2 BDO solver

348 The numerical model used to solve the BDO equation is composed of two parts –
 349 the first solves the modal equation for $\phi(z)$ and c_0 , and determines the values of α and δ ,
 350 and the second evolves the non-dimensional Eq. 9.

351 A fourth order Runge-Kutta integration is used to solve Eqs. A.5 and A.6 for non-
 352 dimensional values of α , δ , c_0 , and the modal function, $\phi(z)$ from an initial stability
 353 profile, $N^2(z)$. For the cosine stability profile these values are $\alpha = 1.03714$, $\delta=0.09318$,
 354 and $c_0=0.33715$, with the corresponding modal function plotted in Figure 1, panel (d).
 355 Eq. A.5 is solved in the region $z \geq 0$ (denoted by the solid line) and then reflected anti-

356 symmetrically to the region $z < 0$ (denoted by the dashed line). The parameter $\eta_0\lambda/h^2$
357 then has a value of 0.3594.

358 In order to test the accuracy of these values, we numerically compute values for
359 α , δ , and c_0 for the sech^2 duct and compare them against their analytically obtained
360 values. The results are presented in Table 1 and demonstrate very good agreement
361 (within 0.04%), lending confidence to the values used for the cosine profile. For the
362 sech^2 duct we use 10,000 grid points over a non-dimensional vertical domain from 0 to
363 100 to allow the stability to asymptote to zero. For our cosine duct we use 10,000 grid
364 points over a vertical range of 0 to 1 since including values of $z > 1$ where the cosine
365 stability profile is strictly zero does not change any of the obtained values.

366 The horizontal time evolution is handled in the same manner as in the NS model
367 described in Section 3.1. The only difference is that instead of time evolving three, 3D
368 quantities, $w(x,t)$, $\theta(x,t)$, and the vertical component of vorticity, $\omega_z(x,t)$, according to the
369 NS equations, the BDO model evolves one, 1D quantity, $A(x,t)$, according to the BDO
370 equation.

371 Finally, in order to compare these results with those of our NS model we compute
372 the displacement field throughout the vertical domain $[-1,1]$. The Boussinesq
373 approximation allows us to assume the dynamics predicted by the BDO equation are
374 vertically anti-symmetric about the center of the duct, $z = 0$, and so we compute the
375 displacement from Eq. 7 for $z = [0,1]$ and reflect it about the center of our domain. With
376 our displacement known we compute the corresponding perturbation to the temperature
377 field by mapping $T(x,z,t)$ to $T(x,z+\eta,t)$ in the region $|z| < 1$. Comparisons between the

378 BDO and NS models consist of comparing the potential temperature fields and we do not
379 compute the vertical velocity field for the BDO prediction.

380 **4 Results**

381 Sections 4.1, 4.2, and 4.3 present the results of both models for soliton and
382 sinusoidal initializations with a range of amplitudes and length scales under inviscid and
383 strictly neutral background stability conditions. Section 4.1 utilizes the soliton
384 initialization (Eq. 16 with $S = 1$) while Section 4.2 uses a soliton-like localized forcing (S
385 $\neq 1$). Section 4.3 utilizes an idealized sine wave initialization. Section 4.4 presents
386 results from the NS model when viscosity is present, and Section 4.5 details the effects of
387 non-zero background stability.

388 Unless otherwise noted all results are reported in a reference frame moving
389 rightward with velocity c_0 . Figures 2, 3, 4, and 6 use markers to track three velocities:
390 the thin vertical line represents the origin in the moving frame and has a velocity c_0 in the
391 stationary frame, the diamonds move leftward with velocity $-c_0$ and represent the origin
392 in the stationary frame. The squares move leftward with velocity $-2c_0$ and represent the
393 point in the stationary frame moving leftward with velocity $-c_0$.

394 **4.1 Soliton Initialization**

395 The soliton initial condition is ideal for comparing the two models as it is the
396 stationary solution predicted by BDO theory. The predicted evolution for each model
397 should then be a strictly horizontal translation of the initial condition. Cases were run for
398 wavelengths λ ranging from 100 to 0.1, with corresponding amplitudes defined by $\eta_0 =$
399 $4\delta/\alpha\lambda$.

400 Figure 2 displays the results of the $\lambda = 25$, $\eta_0 = \sim 0.014$ soliton and is fairly
401 representative of the behavior of solitons with $\lambda \approx 10$ and larger. The horizontal domain
402 size, x_{max} , is 2500 with 1000 grid points and the vertical domain size, z_{max} , is 50 with
403 2501 grid points. The first feature to note is that the bore velocity, given by Eq. 11, is
404 very nearly equal to the long wave phase speed and appears to be nearly stationary. The
405 second noteworthy feature in Figure 2 is the close agreement between the NS and BDO
406 models, with the largest amplitude difference between the two models at about 2.5% of
407 the initial perturbation amplitude. This agreement is highlighted by the inability to
408 distinguish the solid trace of Figure 2 from the dashed trace representing the BDO
409 solution.

410 The dispersive wave train that develops at $x \sim 1250$ propagates leftward at the
411 long wave phase speed (tracking the squares) with an amplitude of about 1% that of the
412 initial perturbation and represents dispersive effects not predicted by the BDO equation.
413 This dispersive wave train owes its existence to the fact that an arbitrary forcing has the
414 potential to excite a variety of different dynamical responses; the soliton forcing is
415 “arbitrary” in the following two ways. The first is that the BDO equation is an
416 approximation, and while its validity is better for the length scales it assumes, it is never a
417 completely accurate representation of the physics being modeled. Because of this, while
418 the soliton is an exact solution of the BDO equation, it cannot also be an exact solution of
419 the NS equations. The emergent dispersive wave then represents motions that the BDO
420 code fails to predict, and that the NS code describes fully.

421 The second effect potentially contributing to this wave is the potential mismatch
422 between the initial temperature and vertical velocity perturbations. The BDO equation is

423 initialized with one quantity, displacement. The NS model, however, requires two fields.
424 Extensive testing not presented here has shown that changing the relative magnitudes of
425 the temperature and velocity perturbations can lead to significant departures from the
426 BDO prediction, with the most striking example being the case of an initial temperature
427 perturbation with no velocity perturbation. In this case the resulting motion was
428 symmetric long-wave disturbances propagating outward from the origin with velocity
429 $\pm c_0$, qualitatively similar to the motion accompanying dropping a stone into a pond. No
430 choice of relative amplitudes completely eliminated the dispersive wave, lending support
431 to the first notion that this wave represents, in part at least, the limitations of the BDO
432 equation.

433 The final effect worth noting is the very small amplitude leftward-travelling wave
434 present at $x = 770$, $t = 136$. This small amplitude perturbation travels with a velocity of
435 $10c_0$ and is the result of the impermeable upper and lower boundaries. This simulation
436 was run with vertical domain sizes of 16, 25, 33.3, 50, 66.67, and 100 and while the
437 soliton and dispersive wave evolution remained unchanged, the velocity of this small
438 scale feature changed according to $V_{\text{feature}} = \sqrt{2} c_0 (z_{\text{max}})^{1/2} \sim 0.47 (z_{\text{max}})^{1/2}$, behavior which
439 is qualitatively similar to that of long waves in shallow water theory. In addition to the
440 BDO equation, Benjamin's paper (1967) also includes a discussion of a system of two
441 immiscible fluids of different densities and depths bounded above and below by
442 impermeable vertical boundaries. That analysis provides the long wave phase speed of
443 waves propagating along the interface between the two fluids, and in our notation with
444 the interface vertically located in the middle of the domain the long wave phase speed is
445 $c_{0,\text{interface}} = 0.5 (z_{\text{max}})^{1/2}$, which is within 6% of our model's values. This 6% discrepancy

446 is likely due to the fact that Benjamin's analysis assumed the interface to be a sharp
447 density discontinuity while our model was run with a region of smoothly varying density
448 (the duct). Furthermore, while the soliton evolution is vertically anti-symmetric about the
449 center of the duct, this long wave feature is not, which supports the interpretation that it is
450 analogous to a surface wave propagating on the interface. This wave is a physical
451 response to unphysical boundary conditions and in light of its small amplitude and
452 apparent lack of influence on the main dynamics considered, we neglect its contribution
453 from this point forward.

454 For wavelengths smaller than 10, the two models begin to diverge more
455 significantly. Results for $\lambda = 5$ are depicted in Figure 3. The horizontal domain size is
456 300 with 3000 grid points and the vertical domain size is 50 with 2501 grid points. The
457 increasingly narrower width of the initial perturbation further violates the assumptions of
458 the BDO equation and the resulting evolution bears this out. The most noteworthy
459 feature in Figure 3 is the dispersive wave train that forms at the origin and propagates
460 leftward with velocity $\sim c_0$. The amplitude of this response is $\sim 3\%$ of the initial
461 perturbation, significantly larger than the dispersive wave of Figure 2. The growing
462 strength of this dispersive component owes its existence to the fact that the BDO soliton
463 is becoming a less accurate approximation for a steady solution of the NS equations for
464 this short length scale (if, indeed, a truly steady solution to the NS equations exists at
465 these scales). Consequently, the initial perturbation excites both a soliton like response
466 and a stronger dispersive wave response.

467 In addition to the growing strength of the dispersive wave, the two predicted
468 evolutions of the BDO soliton begin to differ at this length scale. The NS-evolved soliton

469 clearly lags the BDO prediction. It is no longer meaningful to discuss the amplitude
470 difference between the NS and BDO solitons; they now propagate with different
471 velocities and the leading peak of the difference plot merely highlights this.

472 The $\lambda = 1$ and $\lambda = 0.5$ cases (not shown) represent the lowest values of λ for
473 which the BDO model even qualitatively captures the behavior predicted by the BDO
474 equation. The strength of the dispersive waves continues to grow in amplitude and the
475 predicted soliton geometries and velocities disagree even more strongly for these
476 wavelengths. It is nevertheless remarkable that the qualitative behavior exhibited by the
477 NS solution, namely the emergence of a soliton-like peak, is similar to that predicted by
478 the BDO equation. It is especially remarkable that this qualitative behavior occurs for
479 values of $\lambda \leq h$ when the BDO equation is derived assuming $\lambda \gg h$. At the smallest
480 value evaluated, $\lambda=0.1$, $\eta_0 = \sim 3.5$, the two models diverge wildly. The NS model
481 predicts turbulent breaking while the BDO model, which is a weakly nonlinear theory
482 unable to model such nonlinear features as recirculation regions or breaking, continues to
483 predict horizontal translation of the initial condition. Also, as energy more readily
484 accumulates at smaller scales in the absence of viscosity numerical noise begins to
485 dominate the solution. The addition of viscosity suppresses these small-scale motions,
486 but also removes energy from the dynamics we wish to evaluate more quantitatively.

487 4.2 Soliton-like Initialization

488 In this section we compare results obtained with the BDO and NS codes for a
489 soliton-like initialization, where the value of S in Eq. 16 is different from 1. Again, a
490 number of simulations were performed from which we present a few representative cases.

491 The first case we consider is that of a reduced amplitude displayed in Figure 4,
492 with $\lambda = 10$ and $S = 0.2$, which is representative of all cases with $S < 1.0$, where both the
493 NS and BDO solutions agree fairly well. The horizontal domain size is 1000 with 1000
494 grid points and the vertical domain size is 50 with 5001 grid points. There are two
495 features to consider. The first is the leading peak, which according to both models has a
496 velocity less than the long wave phase speed. This result is to be expected, as the
497 velocity of a soliton is proportional to its amplitude and since the soliton represents the
498 balance between amplitude-dependant nonlinear effects and linear dispersion it follows
499 that reducing the amplitude allows linear dispersion to dominate the perturbation's
500 evolution. The dispersive character is also reflected in the shallow leading edge and the
501 steepened trailing edge of the initial perturbation. The difference in amplitudes predicted
502 by the two models for the $S = 0.2$ case is $\sim 1 \times 10^{-4}$, roughly 2.5% of the peak amplitude of
503 0.004. For the $S = 0.5$ case, the peak amplitude difference is $\sim 2 \times 10^{-4}$, roughly 2% of the
504 peak amplitude of 0.01. The initial dispersive wave with velocity $-c_0$ from Section 4.1 is
505 present as well with an amplitude of $\sim 1\%$ the initial peak amplitude.

506 The second feature we consider is the dispersive wave train trailing the leading
507 peak. The dispersive waves that were seen to develop in Figures 2 and 3 were due to the
508 growing effects of linear dispersion in the NS model due to shorter horizontal length
509 scales of the initial perturbation, which violated the approximations of the BDO theory.
510 Those dispersive waves were not predicted by the BDO equation. The dispersive tail
511 forming in Figure 4, however, is the direct result of an initial perturbation with a
512 decreased amplitude that favors dispersive effects over nonlinear effects, thus both the

513 BDO and NS models predict this dispersion. Finally, we note that dispersive effects
514 increase with decreasing values of S (not shown).

515 Figure 5 displays the results for values of $S > 1$. Panel a) displays the results of a
516 $\lambda = 25$, $S = 10$ initial condition, panel b) shows the evolution of a $\lambda = 25$, $S = 5$ initial
517 condition, and panel c) shows a $\lambda = 10$, $S = 5$ soliton-like perturbation. For the $\lambda = 25$
518 cases, the horizontal domain size is 2500 with 1000 grid points and the vertical domain
519 size is 50 with 2501 grid points. For the $\lambda = 10$ case the horizontal domain size is 1000
520 with 1000 grid points and the vertical domain size is 50 with 5001 grid points. All are
521 plotted with the same horizontal and vertical scale, with the non-dimensional times of
522 each trace listed above. These three cases can be contrasted with one another and reveal
523 three trends. The first is that while none of the three cases display good agreement
524 between the NS and BDO predictions, agreement between the two theories is best for
525 smaller amplitudes, with the $\lambda = 25$, $S = 5$ case displaying better agreement than the other
526 two.

527 The second feature to note is that the time required for independent peaks to
528 emerge from the initial condition is inversely dependent on amplitude, with the $\lambda = 25$, S
529 $= 5$ case requiring almost three times as long as the $\lambda = 25$, $S = 10$ case to begin to
530 develop independent peaks ($T = 816$ of panel b) compared to $T = 272$ of panel a)).

531 The final noteworthy behavior is the dependence of this crest-creation time on the
532 wavelength. The $\lambda = 10$, $S = 5$ case develops peaks at about $T = 102$, which is a factor of
533 8 smaller than the crest creation time of the $\lambda = 25$, $S = 5$ case of $T = 816$. While this
534 behavior may owe its existence more to the differences in amplitude between the $\lambda = 10$
535 and $\lambda = 25$ solitons than it does to the difference in width, it is worth recognizing that

536 neither the $\lambda = 25$, $S = 1$ soliton nor the $\lambda = 10$, $S = 1$ soliton experiences crest separation,
537 so interpreting the difference in width as resulting in a difference in separation time scale
538 for the same pre-factor $S = 5$ is reasonable.

539 4.3 Sinusoidal Initialization

540 *Large amplitude sinusoid*

541 In this section we compare the responses predicted by the BDO and NS codes to
542 initial sinusoidal perturbations described by Eq. 17, focusing on effects due to varying
543 perturbation wavelengths and amplitudes. We begin by presenting the results of each
544 model for a fairly large amplitude perturbation. Figure 6 shows the results of the $\eta_0 =$
545 0.5 , $\lambda = 50$ case. The horizontal domain size is 50 with 1000 grid points and the vertical
546 domain size is 100 with 2501 grid points. The results shown in Figure 6 are qualitatively
547 similar to the other three cases run with $\eta_0 = 0.5$, namely those with $\lambda = 20$, 100, and 200.

548 There are three noteworthy features in Figure 6. The first is that the 2D NS result
549 is quantitatively unreliable because the nonlinear response is very strong, rapidly
550 cascades energy to small scales, and would also excite 3D turbulent motions
551 accompanying overturning if allowed to do so. Our assumption of nearly inviscid
552 motions exacerbates of the numerical noise that arises at smaller scales. A second
553 noteworthy feature is that, despite the problems present in the NS results, it nevertheless
554 predicts nonlinear breaking for this large-amplitude wave. A third noteworthy feature
555 highlights the limits of BDO equation applicability alluded to in Section 4.1 and is the
556 reason for discussing this figure. The BDO equation is a weakly nonlinear theory which
557 predicts crest creation to account for all nonlinear effects. When initialized with a
558 perturbation that leads to overturning and breaking behavior in the NS solution, the BDO

559 response is simply crest creation. This underscores the inherent limits of the BDO
560 equation for large initial perturbation amplitudes.

561 *Wavelength Variations*

562 Reducing the amplitude of the perturbation removes the strongly nonlinear
563 tendencies from the response, such as closed circulations and breaking. Figure 7 displays
564 the results of a $\lambda = 100$, $\eta_0 = 0.1$ perturbation (panel a) and a $\lambda = 200$, $\eta_0 = 0.1$
565 perturbation (panel b) plotted on the same horizontal scale. For $\lambda = 100$ the horizontal
566 domain size is 100 with 1000 grid points, while for $\lambda = 200$ the horizontal domain size is
567 200 with 1000 grid points. Both have a vertical domain size of 100 with 2501 grid
568 points. Other wavelength considered with $\eta_0 = 0.1$ include 50, 20, and 2.

569 Figure 7 highlights five characteristics of the sinusoidal initialization. The first
570 and most obvious is that both the NS and BDO solutions predict a series of amplitude
571 ordered crests, with the larger amplitude peaks leading the smaller. The second is that
572 the NS and BDO results agree fairly well up to the point of crest creation, with both
573 codes predicting roughly the same time for the initial crest emergence. A third
574 characteristic highlighted by Figure 7 is that the time scale over which crests begin to
575 emerge is dependent on the initial perturbation wavelength. Panel a) shows a peak
576 beginning to emerge at $T = 181$ while panel b) predicts a peak emergence at time $T =$
577 363 , twice as long as the $\lambda = 100$ case. This supports the interpretation in Section 4.2 that
578 the length scale plays a role determining the timescale over which individual peaks
579 emerge.

580 A fourth characteristic of the sinusoidal initialization is the relative independence
581 of the emerging crests' geometries on the wavelength. For all perturbation wavelengths,

582 the leading peak develops with a FWHM of ~ 2.5 and an amplitude of ~ 0.25 . This also
583 explains why traces at $T = 363$ and 453 of panel b) appear to be similar to traces at $T =$
584 181 and 272 of panel a); once the peaks emerge, their dynamics are governed by their
585 amplitudes and are no longer dependent on the initial perturbation.

586 The final noteworthy feature of Figure 7 is that the BDO solution noticeably leads
587 the NS prediction. One plausible explanation for this behavior is that since the BDO
588 equation is an approximation that handles nonlinearity solely through crest creation, as in
589 Figure 6, there are additional processes being modeled by the NS equations which may
590 delay the onset of crest creation which the BDO equation fails to capture. Another
591 plausible explanation is that the initial perturbation in the NS model is exciting a
592 dispersive response in addition to the nonlinear response and that this leads to more
593 slowly developing crests. While the exact reasons for this behavior are unknown, this
594 result is consistent with the results presented in Figure 2, Figure 3, and Figure 5.

595 *Amplitude Variations*

596 Again, simulations were run with numerous combinations of λ and η_0 . Figure 8
597 presents the results of a $\lambda = 200$ wave with, $\eta_0 = 0.1, 0.06, 0.03,$ and 0.01 . The horizontal
598 domain size is 200 with 1000 grid points and the vertical domain size is 100 with 2501
599 grid points. Note that the horizontal scale plotted in Figure 8 is twice as large as in
600 Figure 7 and the vertical scale of panel d) is $1/10^{\text{th}}$ that of panels a), b), and c).

601 There are a few noteworthy features highlighted in Figure 8. The first is that as
602 the amplitude of the initial perturbation decreases, the agreement between the NS and
603 BDO results improves. A second is that as the amplitude of the initial perturbation
604 decreases the emergence time of the initial crest increases in a very consistent manner:

605 reducing the initial amplitude by a factor of 0.6 increases the emergence time by a factor
606 of $\sim 1/0.6 (=1.667)$, reducing the initial amplitude by a factor of 0.3 increases the
607 emergence time by a factor of $\sim 1/0.3 (=3.333)$, and reducing the initial amplitude by a
608 factor of 10 increases the emergence time by a factor of ~ 8.5 , though with the large time
609 scales involved in panel d) it becomes more difficult to define the “crest creation” time.
610 A third noteworthy feature seen in Figure 8 is that the geometry of the emerging peaks is
611 strongly dependent on the perturbation amplitude. Unlike Figure 7, where the emergent
612 peaks are relatively similar, there is a noticeable trend for smaller and broader peaks to
613 emerge as the initial perturbation amplitude is decreased.

614 Finally, the apparent sub- c_0 velocity of the leading peak of panel d) needs to be
615 addressed. This behavior, with the leading emergent peak lagging the long-wave phase
616 speed, was observed in a number of runs where the leading emergent peak had a width
617 comparable to the initial perturbation wavelength. It is possible, though unconfirmed at
618 the moment, that this behavior is due to the periodicity of the forcing. The horizontal
619 domain is periodic, and so the evolution depicted in Figure 8 is really the evolution of a
620 segment of an infinitely long wave train. It is reasonable to expect that the tail of the
621 evolution, which is long relative to the horizontal domain, will wrap around and interact
622 with the leading peak, and that the sum of these two effects is a peak which travels with
623 velocity less than the long-wave phase speed. That both the NS and BDO models predict
624 this behavior supports this notion, as does the fact that this behavior was seen for a
625 variety of amplitudes and wavelengths when the emergent peak was of comparable width
626 to the horizontal domain. Fully testing this would require initializing the model with an

627 isolated sine wave, though the observed behavior might be expected for a real sine wave
628 initialization allowing nonlinear evolutions at successive crests.

629 4.4 Viscous effects

630 We considered the effects of viscosity for a variety of length scales and
631 amplitudes for both sinusoidal and soliton-like initial conditions. The results were fairly
632 uniform in the sense that every simulation exhibited the same general effects.

633 Unsurprisingly, the addition of viscosity acted to remove energy from the response, as in
634 Figure 9, which displays the results of a $\lambda = 200$, $\eta_0 = 0.1$ sine wave in the presence of
635 zero viscosity (dashed line) and non-zero viscosity (solid line). The horizontal domain
636 size is 200 with 1000 grid points and the vertical domain size is 100 with 2501 grid
637 points. The addition of viscosity did have an unexpected effect on the resulting
638 dynamics. While the amplitude of the leading crest in Figure 9 is smaller than in the
639 inviscid case, it nevertheless leads the inviscid crest. The role viscosity plays in causing
640 the peak to lead the inviscid case is not yet understood, though examining the dispersion
641 relation with viscous terms retained may explain this behavior.

642 A practical implication of the role of viscosity is that it acts as a filter on those
643 initial conditions that will initiate observable bores. As seen in previous sections,
644 increasing the perturbation wavelength and decreasing the amplitude both act to increase
645 the time over which crest creation occurs. As that time increases, viscous effects become
646 increasingly important in determining whether a bore will develop or whether energy
647 dissipation will prevent bore formation.

648 4.5 Non-zero background stability

649 In this final section we examine the effects of non-zero stability surrounding the
650 thermal duct. In an effort to more closely model the real atmosphere, we retain the
651 addition of viscosity from Section 4.4. Additional runs with zero viscosity (not presented
652 here) demonstrate similar qualitative responses to the results discussed in this section. A
653 stable atmosphere allows for vertical wave propagation and we expect that increasing the
654 background stability will allow initial perturbation energy to leak away from the duct,
655 potentially decreasing or preventing crest creation and bore formation. A number of
656 simulations were performed with $N_B^2 = 1, 0.5, 0.1, 0.05, 0.01, 0.005, 0.001, 0.0005,$ and
657 0.0001 . Figure 10 displays the results of a $\lambda = 100, \eta_0 = 0.1$ wave for $N_B^2 = 0.01$ (panel
658 a) and $N_B^2 = 0.1$ (panel b). The horizontal domain size is 100 with 1000 grid points and
659 the vertical domain size is 100 with 2501 grid points. The dashed lines are the strictly
660 neutral stability case, $N_B^2 = 0.0$.

661 The general trend is that increasing background stability decreases peak
662 amplitudes, with the $N_B^2 = 0.01$ case being the smallest for which emergent peaks grew
663 and subsequently decreased in amplitude. As the background stability increases further,
664 the perturbation at the thermal duct decreases to the point at which there is not sufficient
665 energy to drive nonlinear crest creation. This result is shown both in panel b) of Figure
666 10, with $N_B^2 = 0.1$ and in Figure 11, which is a stationary-frame, partial-domain, false
667 color image (blue is cold, red is hot) of the potential temperature perturbation. The
668 radiation of energy away from the duct is clear from the tilted bands in Figure 11.

669 The effect of non-zero stability on bore formation was also examined in
670 Laughman, et al. (2009b). There it was hypothesized that the inhibiting effect of energy
671 radiating away from the duct could be countered by increasing the initial perturbation

672 amplitude, providing a sufficient amplitude over the necessary time scale to allow crest
673 creation. This concept is revisited here, with results presented in Figures 12 and 13. Here
674 the amplitude of the wave in Figure 10 panel b) is increase by a factor of three. Both the
675 line plot of Figure 12 and the full-field false color image of Figure 13 demonstrate that
676 the hypothesis of Laughman et al. (2009b) is correct.

677 The line plot displays a number of noteworthy features of the $\eta_0 = 0.3$ case (solid
678 line), especially when contrasted with the $\eta_0 = 0.1$ case (dashed line) of Figure 11. The
679 first is that the increased amplitude does indeed allow crest creation. Additionally, the
680 peaks occurring for $\eta_0 = 0.3$ are narrower than previous, smaller amplitude, cases (i.e.
681 Figure 7 and Figure 8), confirming the result of Section 4.3 that peak geometry is
682 dependent on the perturbation amplitude. Finally, the amplitudes of the leading peaks
683 decay rapidly, an effect which is partially due to viscous dissipation and possibly due to
684 other dynamic effects such as dispersion.

685 Figure 13 is a stationary-frame, partial-domain, false color image of the potential
686 temperature field and provides a more complete picture of the resulting dynamics
687 presented in Figure 12. The nonlinear response centered at the duct remains significantly
688 stronger than the radiative response throughout the vertical domain. Furthermore, as
689 early as $T = 91$ (panel b) the individual peaks form and are seen to modify the long wave
690 radiation field of Figure 11. As the horizontal scale of the response at the duct decreases,
691 k increases which, for constant N^2 , results in a smaller m and larger λ_z . The crests arising
692 in Figure 13 are sufficiently narrow that the m^2 computed by Eq. 15 in the region above
693 and below the duct is negative, resulting in an evanescent response in that region. The
694 effect of this evanescent perturbation is seen in the modulation of the long wave radiation

695 beginning at time $T = 91$ and is clearest at time $T = 453$. The question of whether or not
696 a bore can form in the presence of a given background stability may then simply be
697 whether or not the initial perturbation has sufficient amplitude to create crests that are
698 sufficiently narrow as to have a negative m^2 in the region away from the duct and be
699 trapped, though this remains to be examined further.

700 There is one final concern to address for the case of $N_B^2 \neq 0.0$. The vertical
701 boundaries are impermeable, and will necessarily reflect energy back into the domain,
702 potentially leading to unphysical results. This was not an issue in Sections 4.1 to 4.4
703 where the only effect of these boundaries was the vanishingly small amplitude, fast,
704 linear wave response. Here, however, the background stability allows for a significant
705 portion of the initial wave energy to propagate to the boundaries and reflect back to the
706 ducting region. Similar behavior was previously examined and seen to lead to unphysical
707 dynamics (see Laughman et al., 2009b). Concern that the structure of the response seen
708 in Figures 12 and 13 might somehow be an artifact of this reflection led to the $N_B^2 = 0.1$,
709 $\eta_0 = 0.3$, $\lambda = 100$ simulation being rerun in a vertical domain that was 8 times larger. The
710 results of that simulation are qualitatively identical to those presented here; the number of
711 peaks, as well as the general shape of the evolution, is the same while actual peak
712 amplitudes vary by as much as 14%. While these results confirm the qualitative validity
713 of the NS model for these environments they also demonstrate that caution must be used
714 in the quantitative application of this model to observation.

715 **5 Summary and Conclusions**

716 We have employed two codes solving the Boussinesq Benjamin-Davis-Ono
717 (BDO) equation and the 2D Boussinesq Navier-Stokes (NS) equations to describe

718 responses to various initial perturbations to an idealized thermal duct at MLT altitudes.
719 Initial perturbations having soliton and sinusoidal forms with varying scales and
720 amplitudes were considered. Also examined were the influences of viscosity and non-
721 zero stability away from the thermal duct. Initial conditions and environments for which
722 the assumptions of the BDO theory are valid yield very good agreement between the
723 BDO and NS solutions extending to late times. However, initial conditions and
724 environments that violate BDO assumptions to varying degrees lead (as might be
725 expected) to departures of the two solutions in form and with time, with the larger
726 disparities occurring for the more significant violations of BDO assumptions. Viscosity
727 and non-zero stability away from the thermal duct, which are not considered in the simple
728 BDO theory, were likewise found to lead to significant departures of the NS solutions
729 from predictions of BDO theory. Specific differences between the BDO and NS solutions
730 for the various cases considered, summarized below, suggest that applications of BDO
731 theory in interpretations of MLT bore observations may cause errant inferences of bore
732 dynamics and environments, even for relatively simple cases in which only thermal
733 ducting needs to be considered.

734 For idealized environments, *i.e.*, those having zero background stability away
735 from the thermal duct and no viscous dissipation, as well as large spatial scales and
736 weakly nonlinear forcing, BDO solutions are found to closely approximate the NS
737 solutions, even when dispersive effects dominate nonlinear effects. Initial solitons having
738 smaller spatial scales, however, are found to cause increasing departures of NS solutions
739 from BDO predictions. As the initial soliton length-scale, $\lambda = 4\delta/\alpha\eta_0$, decreases, the NS

740 solution exhibits a smaller amplitude than the BDO solution, a slower phase speed (but
741 still exceeding the maximum linear phase speed, c_0), and a dispersive trailing wave train.

742 Initial soliton-like perturbations (having a soliton shape, but smaller amplitudes
743 than required to balance dispersive and nonlinear effects) yield BDO and NS solutions
744 that remain in close agreement, even for relatively small wavelengths, because the
745 weakly-nonlinear assumption of the BDO theory is valid. However, initial perturbations
746 having a soliton shape, but larger amplitudes, yield BDO and NS solutions that differ
747 dramatically because the weakly nonlinear assumption of BDO theory is strongly
748 violated. In these cases, the BDO solutions exhibit higher phase speeds and much more
749 rapid crest creation than is seen in the NS solutions.

750 We also explored the evolutions of bore responses to initial long-wavelength
751 sinusoidal perturbations in the BDO and NS solutions, given the evidence for such
752 sources in mesospheric bore observations. In these cases, the two solutions agree well
753 where the BDO weakly nonlinear (small-amplitude) assumption is satisfied. As the initial
754 sinusoidal amplitude increases, however, departures of the BDO response from the NS
755 response become more pronounced, with comparable crest spacing in the two solutions,
756 but with higher phase speeds and somewhat faster crest creation occurring in the BDO
757 solutions.

758 Figure 14 summarizes the observed relationship between crest creation timescale
759 with both amplitude and wavelength for the sinusoidal perturbation. General tendencies
760 seen to occur for both soliton-like and sinusoidal initial perturbations in the BDO and NS
761 solutions can be summarized as follows:

762 ∞ the crest-creation timescale is proportional to the length scale of the perturbation,

763 ∞ the crest-creation timescale is inversely proportional to perturbation amplitude,
764 ∞ the geometry of the emergent crests is dependent on the perturbation amplitude,
765 ∞ the geometry of the emergent crests is independent of the perturbation
766 wavelength,
767 ∞ agreement between the BDO and NS solutions is better for smaller amplitudes
768 and larger length scales,
769 ∞ departures of BDO predictions from NS solutions are most pronounced for
770 strongly nonlinear responses, and
771 ∞ both BDO predictions and 2D NS solutions fail to describe bore responses when
772 nonlinearity is sufficiently strong to induce recirculation, overturning, instability,
773 and 3D turbulence.

774 Comparisons of NS solutions obtained with negligible and non-negligible
775 viscosity indicate that rapid viscous dissipation suppresses crest creation and causes the
776 leading peak to advance beyond that of the inviscid case, suggesting that molecular and
777 turbulent dissipation may impact bore evolutions and their interpretations for scales and
778 altitudes at which these effects are non-negligible. Background stratification that enables
779 an initial sinusoidal perturbation to propagate away from the thermal duct results in rapid
780 depletion of perturbation energy at the thermal duct and weak or no nonlinear steepening
781 and crest creation. Weaker background stratification does not suppress steepening and
782 crest creation entirely, but it does weaken the crests that do arise. Stronger forcing can
783 offset these tendencies to some extent, but nonlinear steepening and crest creation exhibit
784 a qualitatively different evolution with background stratification than predicted for the
785 same initial perturbation in the absence of background stratification. For large initial

786 perturbation amplitudes, crests may evolve more rapidly with than without background
787 stratification, but they also exhibit smaller crest separations, leading-crest amplitude
788 decay, and bore responses extending to higher and lower altitudes not seen to occur for
789 zero background stratification. We note that similar insights may be drawn from work
790 that extends the scope of the BDO equation to include similar viscous and radiative
791 effects, but that we are not in a position to comment on those extensions since we have
792 not incorporated them into our current BDO model.

793 To relate our results to bore observations at MLT altitudes, we note that a length
794 scale of 5 km implies a $\lambda = 100$ perturbation that corresponds to an initial perturbation
795 wavelength of 500 km. Our time scale of ~ 19 sec implies initial crest formation after ~ 1
796 hr and a series of ~ 3 -5 amplitude-ordered crests over the next 2 hr. The separations
797 between crests are variable, with a largest separation of ~ 70 km, a minimum separation of
798 ~ 37 km, and crest FWHM of ~ 20 km. The corresponding long-wave phase speed is ~ 88
799 ms^{-1} and the bore phase speed is ~ 90 - 95 ms^{-1} . A longer initial wavelength (~ 1000 km)
800 and a smaller initial amplitude (by ~ 2) results in crest creation after ~ 3 hr, ~ 3 -5 crests
801 over the next ~ 2 hr, and crest FWHM of ~ 25 km. While a duct FWHM of 5 km is on the
802 order of a scale height, these values obtained with the Boussinesq approximation
803 nevertheless compare favorably to observed bores (Medieros et al., 2001; Batista et al.,
804 2002; Chung et al., 2003; Smith et al., 2003, 2005; She et al., 2004; Fehine et al., 2005,
805 2009; Shiokawa et al., 2006; Snively et al., 2005; Taylor et al., 1995), though specific
806 bore parameters will depend on the environmental parameters relevant to each
807 observation.

808 We anticipate that future efforts will address a further quantification of the
809 relationships between environmental parameters and initial conditions and the bore
810 characteristics that arise, including the roles of background stratification and horizontal
811 winds. The initial examination of bores arising due to Doppler ducting by Laughman et
812 al. (2009b) demonstrated that these should also be important in the MLT, where much of
813 the small-scale structure in the vertical also has large horizontal scales due to the
814 dominance of the motion spectrum in many cases by inertia-gravity wave motions. Such
815 future work will make continued use of the BDO equation, both for the comparison it
816 offers the NS predictions as well as the simplified insights it offers to the dynamics.

817 **A Appendix A: BDO details**

818 This appendix contains additional details regarding the BDO equation, including
819 formulae for computing α , δ , c_0 , and $\phi(z)$. Recall that $\eta(x,z,t)$ can be decomposed into
820 two functions,

$$821 \eta(x, z, t) = A(x, t) \phi(z) \quad (A.1)$$

822
823
824 The modal function, $\phi(z)$, and the long wave phase speed, c_0 , are the solutions of
825 the non-Boussinesq modal equation (Ono, 1975),

$$826 \frac{d}{dz} \left\{ \rho_0(z) \frac{d\phi(z)}{dz} \right\} - \frac{g}{c_0^2} \frac{d\rho_0(z)}{dz} \phi(z) = 0 \quad (A.2)$$

827
828
829 where g is acceleration due to gravity and $\rho_0(z)$ is the unperturbed density profile. The
830 unperturbed density is defined as

831

$$\rho_0(z) = \begin{cases} \rho_0 (= \text{const}), & |z| > h \\ \rho_0(z), & |z| \leq h \end{cases} \quad (\text{A.3})$$

833

834 Using the definition for the buoyancy frequency,

835

$$N^2(z) = -\frac{g}{\rho_0(z)} \frac{d\rho_0(z)}{dz} \quad (\text{A.4})$$

837

838 and the Boussinesq approximation we rewrite Eq. A.2 as

839

$$\frac{d^2\phi(z)}{dz^2} + \frac{N^2(z)}{c_0^2}\phi(z) = 0 \quad (\text{A.5})$$

841

842 which is an eigenvalue problem that can then be solved for the eigenvalue c_0 and

843 corresponding eigenfunction $\phi(z)$. There are three conditions imposed on $\phi(z)$:

844 $\phi(0)=0$, $\phi(h)=1$, and $\phi'(h)=0$ (Ono, 1975). We note that the lowest-order eigenfunction

845 corresponds to the largest eigenvalue c_0 , and as it is this lowest mode that dominates

846 observation we, like some past authors, restrict our study to this the lowest mode.

847 Formulae for computing α and δ can be found in Grimshaw (1980) and rewritten

848 subject to inviscid and incompressible approximations, yielding

849

$$I\alpha = 3 \int_0^\infty \rho_0 c_0^2 \left(\frac{\partial\phi(z)}{\partial z} \right)^3 dz \quad (\text{A.6a})$$

851

$$I\delta = \lim_{z \rightarrow \infty} c^2(\rho_0\phi^2) \quad (\text{A.6b})$$

853

$$I = 2 \int_0^{\infty} \rho_0 c_0 \left(\frac{\partial \phi(z)}{\partial z} \right)^2 dz \quad (\text{A.6c})$$

855

856 With α , δ , and c_0 defined, the evolution equation for $A(x,t)$ can be written as

857

$$\frac{\partial A}{\partial t} + c_0 \frac{\partial A}{\partial x} + \alpha A \frac{\partial A}{\partial x} + \delta \frac{\partial^2}{\partial x^2} H(A) = 0 \quad (\text{A.7})$$

859

860 which is the BDO equation. $\mathcal{H}(A)$ is the Hilbert transform of A , defined as

861

$$H[A(x)] = \frac{1}{\pi} \int_{-\infty}^{\infty} \frac{A(x')}{x' - x} dx' \quad (\text{A.8})$$

863

864 This definition is used by authors such as Christie (1989), but is not a uniformly accepted

865 definition, and other authors such as Ono (1975) define $\mathcal{H}(A)$ as $-\mathcal{H}(A)$. This sign866 ambiguity also leads some authors to compute δ in Eq. A.6 as $-\delta$.

867 As the limits of integration in Eq. A.6 indicate, there are two regions to consider

868 when using the BDO equation. Figure 1 (panel b) depicts both the inner region where the

869 density changes with altitude, and the outer region where the density is a constant. Fluid

870 displacement in the inner region, $[0,h]$, is given by Eq. A.1, while displacement in the871 outer region, $[h,\infty]$, can be computed from

872

$$\eta(x, z, t) = \int_{-\infty}^{\infty} \mathcal{F}(A) \exp[-ikx - |k|(z - h)] dk \quad (\text{A.9})$$

874

875 Where \mathcal{F} is a linear operator defined by

876

$$877 \quad \mathcal{F}(A) = \frac{1}{2\pi} \int_{-\infty}^{\infty} A(x,t) \exp(ikx) dx \quad (\text{A.10})$$

878

879 We now illustrate the above theory for the sech^2 duct, which is convenient and
880 insightful due to its analytic nature. The sech^2 stability profile corresponds to a
881 hyperbolic tangent density profile. Again, we examine the upper half plane as depicted in
882 Figure 1 (panel b).

883 The sech^2 profile also has the property of asymptoting to a value of 1 as z tends to
884 infinity. In order to strictly satisfy the definition given by Eq. A.3, this would define an h
885 for the inner region that is infinitely large. A more useful treatment is to instead define h
886 by $N^2(z) = \text{sech}^2(z/h)$ (Benjamin, 1967; Christie, 1988). Substituting $N^2(z) = \text{sech}^2(z/h)$
887 into Eq. 5 and Eq. 6 yields $c_0 = 2^{-1/2} N_0 h$, $\alpha = 6/5 c_0/h$, and $\delta = 3/4 c_0 h$. These are the
888 analytically obtained values presented in table 1 of Section 3.

889 Substituting these values into Eq. A.7 then yields the correct evolution equation
890 for finite-amplitude long-wave perturbations to the fluid field in the presence of a sech^2
891 density stratification.

892 **Acknowledgments**

893 This research was supported by NSF grants ATM-0924802, ATM-0314060, and ATM-
894 0836407. The authors also thank three anonymous reviewers for their comments,
895 corrections, and insights.

896 **References**

897 Airy, G. B.: Tides and Waves, *Encyclopaedia Metropolitana*, London, 1845

898 Batista, P. P., Clemesha, B. R., Simonich, D. M., Taylor, M. J., Takahashi, H., GOBBI,
899 D., Batista, I. S., Buriti, R. A., Medeiros, A. F.: Simultaneous lidar observation of a
900 sporadic sodium layer, a "wall" event in the OH and OI5577 airglow images and the
901 meteor winds., *J. of Atmospheric and Solar-Terrestrial Physics*, **64**, 1327 - 1335,
902 2002.

903 Benjamin, T. B.: Internal wave of permanent form in fluids of great depth, *J. Fluid*
904 *Mech.*, **29**, 559, 1967.

905 Christie, D. R.: Long nonlinear waves in the lower atmosphere. *J. Atmos. Sci.*, **46**, 1462-
906 1490, 1989.

907 Chung, J.-K., Y. H. Kim, and Y.-I. Won: Observations of mesospheric waves with an all-
908 sky camera in Korean Peninsula, *Adv. Space Res.*, **32**(5), 825-830, 2003.

909 Davis, R. E., and Arcivos, A.: Solitary internal waves in deep water, *J. Fluid Mech.*, **29**,
910 593-607, 1967.

911 Dewan, E. M., and R. H. Picard: Mesospheric bores, *J. Geophys. Res.*, **103**(D6), 6295-
912 6305, 1998.

913 Dewan, E.M., and R. H. Picard: On the origin of mesospheric bores, *Journal of*
914 *Geophysical Research*, **106**, 2921 – 2928, 2001.

915 Fechine, J., Medeiros, A.F., Buriti, R.A., Takahashi, H., Gobbi, D.: Mesospheric bore
916 events in the equatorial middle atmosphere. *Journal of Atmospheric and Solar-*
917 *Terrestrial Physics*. **67**, 1774 - 1778, 2005.

918 Fechine, J., C. M. Wrasse, H. Takahashi, A. F. Medeiros, P. P. Batista, B. R. Clemesha,
919 L. M. Lima, D. Fritts, B. Laughman, M. J. Taylor, P. D. Pautet, M. G. Mlynczak, J.

920 M. Russell: First observation of an undular mesospheric bore in a Doppler duct, *Ann.*
921 *Geophys.*, **27**, 1399-1406, 2009.

922 Fritts, D. C., C. Bizon, J. A. Werne, and C. K. Meyer: Layering accompanying turbulence
923 generation due to shear instability and gravity wave breaking, *J. Geophys. Res.*, **108**,
924 D8, 8452, doi:10.1029/2002JD002406, 2003.

925 Fritts, D. C., S. L. Vadas, K. Wan, and J. A. Werne: Mean and variable forcing of the
926 middle atmosphere by gravity waves, *J. Atmos. Solar-Terres. Phys.*, **68**, 247-265,
927 2006.

928 Fritts, D. C., L. Wang, J. Werne, T. Lund, K. Wan: Gravity wave instability dynamics at
929 high Reynolds numbers, 1: Wave field evolution at large amplitudes and high
930 frequencies, *J. Atmos. Sci.*, **66**, 1126-1148, doi:10.1175/2008JAS2726.1., 2009a

931 Fritts, D. C., L. Wang, J. Werne, T. Lund, and K. Wan: Gravity wave instability
932 dynamics at high Reynolds numbers, 2: Turbulence evolution, structure, and
933 anisotropy, *J. Atmos. Sci.*, **66**, 1149-1171, doi:10.1175/2008JAS2727.1., 2009b

934 Grimshaw, R.: Solitary waves in a compressible fluid. *Pageoph*, **119**, 780-797, 1980.

935 Hammack, J. L., and H. Segur: The Korteweg-de Vries equation and water waves. Part
936 2: Comparison with experiments. *J. Fluid Mech.*, **65**, 289-314, 1974.

937 Koop, C. G., Butler, G.: An investigation of internal solitary waves in a two-fluid system.
938 *J. Fluid Mech.*, **112**, 225-251, 1981

939 Korteweg, D. J., and de Vries, F.: On the change of form of long waves advancing in a
940 rectangular canal, and on a new type of long stationary waves. *Philosophical*
941 *magazine*. **39-40**, 421-444, 1895.

942 Lamb, H. *Hydrodynamics*, 6th Edition. Cambridge University Press, 1932

943 Laughman, B., *Numerical modeling of mesospheric bores*, Ph. D. Thesis, University of
944 Colorado, Boulder. U.S.A., 2009a

945 Laughman, B., D. C. Fritts, and J. Werne: Numerical simulation of bore generation and
946 morphology in thermal and Doppler ducts, *Ann. Geophys.*, **27**, 511-523, 2009b

947 Lighthill, J., *Waves in Fluids*, Cambridge Univ. Press, New York, 1978.

948 Maslowe, S. A., Redekopp, L. G.: Long nonlinear waves in stratified shear flows, *J. Fluid*
949 *Mech.*, **101**, 321-348, 1980.

950 Medeiros, A. F., Taylor, M. J., Takahashi, H., Batista, P. P., Gobbi, D.: An unusual
951 airglow wave event observed at Cachoeira Paulista 23oS, *Advances in Space*
952 *Research*, **27**, 1749 - 1754, 2001.

953 Miles, J. W.: The Korteweg-de Vries equation: a historical essay. *J. Fluid. Mech.*, **106**,
954 131-147, 1981.

955 Ono, H.: Algebraic solitary wave in stratified fluids, *J. Phys. Soc. Jpn.*, **39**, 1082-1091,
956 1975.

957 Porter, A. and Smyth, N.: Modelling the morning glory of the Gulf of Carpentaria. *J.*
958 *Fluid Mech.* **454**, 1-20, 2002

959 Rayleigh, Lord, Note on tidal bores, *Proc. R. Soc. London A*, **81**, 448-449, 1908.
960 Reprinted in *Scientific Papers by Lord Rayleigh*, **5**, 495, Pap. 333, Dover, Mineola,
961 N.Y., 1964.

962 Seyler, C. E.: Internal wave and undular bores in mesospheric inversion layers. *J.*
963 *Geophys. Res.*, **110**, D09S05, doi:10.1029/2004JD004685, 2005.

964 She, C. Y., Li, T., Williams, B. P., Yuan, T., Picard, R. H.: Concurrent OH imager and
965 sodium temperature/wind lidar observation of a mesopause region undular bore event

966 over Fort Collins/Platteville, Colorado. *Journal of Geophysical Research*, **109**, 22107
967 - 22115, 2004.

968 Shiokawa, K., Suzuki, S., Otsuka, Y., Ogawa, T., Nakamura, T., Mlynczak, M. G.,
969 Russell III, M. J.: A Multi-Instrument Measurement of a Mesospheric Front-Like
970 Structure at the Equator. *Journal of the Meteorological Society of Japan*, **84**, 305 -
971 316, 2006.

972 Smith, S. M., Taylor, M. J., Swenson, G. R., She, C. Y., Hocking, W., Baumgardner, J.,
973 Mendillo, M.: A multidagnostic investigation of the mesospheric bore phenomenon.
974 *Journal of Geophysical Research*, **108**, 1083 - 1101, 2003.

975 Smith, S., Friedman, M. J.; Raizada, S.; Tepley, C.; Baumgardner, J., Mendillo, M.
976 Evidence of mesospheric bore formation from a breaking gravity wave event:
977 simultaneous imaging and lidar measurements. *Journal of Atmospheric and Solar-*
978 *Terrestrial Physics*, **67**, 345 – 356, 2005.

979 Snively, J. B., and V. P. Pasko: Antiphase OH and OI airglow emissions induced by a
980 short-period ducted gravity wave, *Geophys. Res. Lett.*, **32**, L08808,
981 doi:10.1029/2004GL022221, 2005.

982 Spalart, P.R., Moser, R. D., and Rogers, M. M.: Spectral Methods for the Navier-Stokes
983 Equations with One Infinite and Two Periodic Directions. *J. Comput. Phys.* **96**, 297-
984 324, 1991.

985 Taylor, M. J., D. N. Turnbull, and R. P. Lowe: Spectrometric and imaging measurements
986 of a spectacular gravity wave event observed during the ALOHA-93 campaign,
987 *Geophys. Res. Lett.*, **22**, 2848-2852, 1995.

988 Werne, J. A., and D. C. Fritts: Stratified shear turbulence: Evolution and statistics,
 989 *Geophys. Res. Lett.*, **26**, 439-442, 1999.

990 Werne, J. A., and D. C. Fritts: Anisotropy in a stratified shear layer , *Phys. Chem. Earth*,
 991 **26**, 263-268, 2001.

992 **Tables**

	Analytic Value	Numerical Value	% difference
α	0.848528	0.848276	0.0297 %
δ	0.530330	0.530361	0.0057 %
c_0	0.707107	0.706842	0.0375 %

993

994 **Table 1:** Analytically and numerically obtained values of α , δ and c_0 for the sech^2
 995 stability profile.

996 **Figure Captions**

997 **Figure 1:** Panels (a) and (b): Density profiles considered by the BDO equation. Panel
 998 (c): Raised cosine stability profile used in our models. The dashed lines of panel (c)
 999 mark the FWHM of the cosine duct from $-h/2$ to $h/2$. Panel (d): Modal function for the
 1000 cosine stability profile computed for $z \geq 0$ (solid line) and anti-symmetrically reflected to
 1001 the region $z < 0$ (dashed line).

1002 **Figure 2:** Time evolution of a $\lambda = 4\delta/\alpha\eta_0 = 25$ soliton depicted in a reference frame
 1003 moving with the long wave phase speed $c_0 = 0.33715$. The upper panel displays the
 1004 horizontally averaged potential temperature predicted by the NS (solid trace) and BDO
 1005 (dashed trace) equations. The lower panel plots the difference between the NS and BDO

1006 solutions (NS minus BDO). The diamond moves leftward with velocity c_0 and represents
1007 the origin in the stationary frame. The square moves leftward with velocity $-2c_0$ and
1008 represents the point moving leftward with the long wave phase speed in the stationary
1009 frame.

1010 **Figure 3:** Time evolution of a $\lambda = 5$ soliton depicted in a reference frame moving with
1011 the long wave phase speed $c_0 = 0.33715$. Panel (a) displays the horizontally averaged
1012 potential temperature predicted by the NS (solid trace) and BDO (dashed trace)
1013 equations. Panel (b) plots the difference between the NS and BDO solutions (NS minus
1014 BDO).

1015 **Figure 4:** Time evolution of a $\lambda = 10$, $S = 0.2$ perturbation shown in a reference frame
1016 moving with the long-wave phase speed $c_0 = 0.33715$. Displayed are the horizontally
1017 averaged potential temperature predicted by the NS (solid trace) and BDO (dashed trace)
1018 equations.

1019 **Figure 5:** Time evolution of three soliton-like initial conditions defined by Eq. 16. Non-
1020 dimensional times are listed above each trace. Panel a) shows the results of a $\lambda = 25$, $S =$
1021 10 perturbation. Panel b) shows the results of a $\lambda = 25$, $S = 5$ perturbation. Panel c)
1022 shows the results of a $\lambda = 10$, $S = 5$ perturbation. Displayed are the horizontally-
1023 averaged potential temperature predicted by the NS (solid trace) and BDO (dashed trace)
1024 equations.

1025 **Figure 6:** Time evolution of a $\lambda = 50$ $\eta_0 = 0.5$ sinusoidal perturbation. The solid line is
1026 the NS solution and the dashed line is the BDO solution.

1027 **Figure 7:** Panel a) time evolution of a $\lambda = 100$ $\eta_0 = 0.1$ sinusoidal perturbation. Panel b)
1028 time evolution of a $\lambda = 200$ $\eta_0 = 0.1$ sinusoidal perturbation. The solid line is the NS

1029 solution and the dashed line is the BDO solution. Both horizontal and amplitude scales
1030 are the same.

1031 **Figure 8:** Time evolution of a $\lambda = 200$ perturbation with amplitude a) $\eta_0 = 0.1$, b) $\eta_0 =$
1032 0.06 , c) $\eta_0 = 0.03$, and d) $\eta_0 = 0.01$. Note that the scale of panel d) is a factor of 10
1033 smaller than panels a), b), and c). The solid line is the NS solution and the dashed line is
1034 the BDO solution.

1035 **Figure 9:** Time evolution of a $\lambda = 200$ $\eta_0 = 0.1$ sinusoidal perturbation in the presence of
1036 viscosity. The solid line is the NS solution and the dashed line is the NS solution in the
1037 absence of viscosity.

1038 **Figure 10:** Evolution of a $\lambda = 100$ $\eta_0 = 0.1$ sine wave perturbation in the presence of a
1039 non-zero background stability (solid line) and in the presence of a strictly neutral
1040 background (dashed line). The background stability in panel a) is $N_B^2 = 0.01$ and the
1041 stability in panel b) is $N_B^2 = 0.1$.

1042 **Figure 11:** Evolution of a $\lambda = 100$ $\eta_0 = 0.1$ sine wave perturbation in the presence of a
1043 non-zero background stability $N_B^2 = 0.1$. Displayed is the false colored perturbation
1044 potential temperature field at six different times. Blue represents colder denser fluid
1045 while red represents warmer less dense fluid.

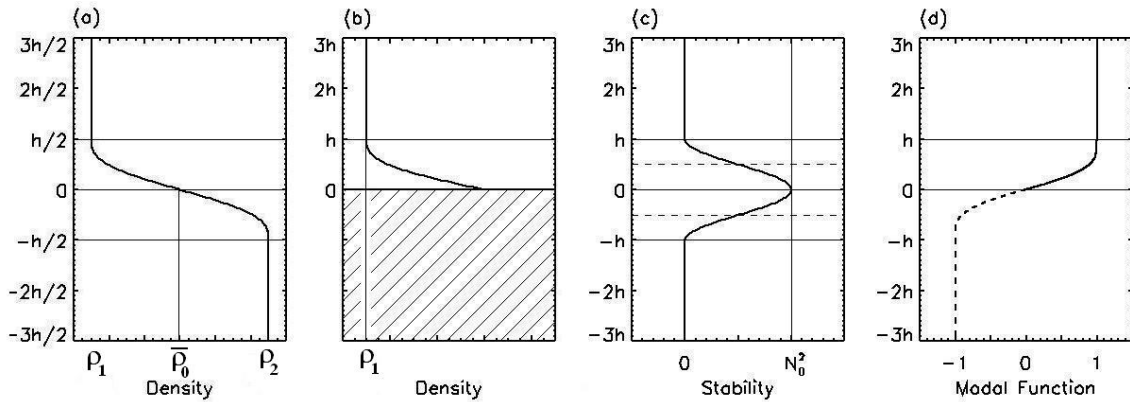
1046 **Figure 12:** Evolution of a $\lambda = 100$ $\eta_0 = 0.3$ sine wave perturbation (solid line) and a $\lambda =$
1047 100 $\eta_0 = 0.1$ sine wave perturbation (dashed line) in the presence of a non-zero
1048 background stability $N_B^2 = 0.1$.

1049 **Figure 13:** Evolution of a $\lambda = 100$ $\eta_0 = 0.3$ sine wave perturbation in the presence of a
1050 non-zero background stability $N_B^2 = 0.1$. Displayed is the false colored perturbation

1051 potential temperature field at six different times. Blue represents colder denser fluid
 1052 while red represents warmer less dense fluid.

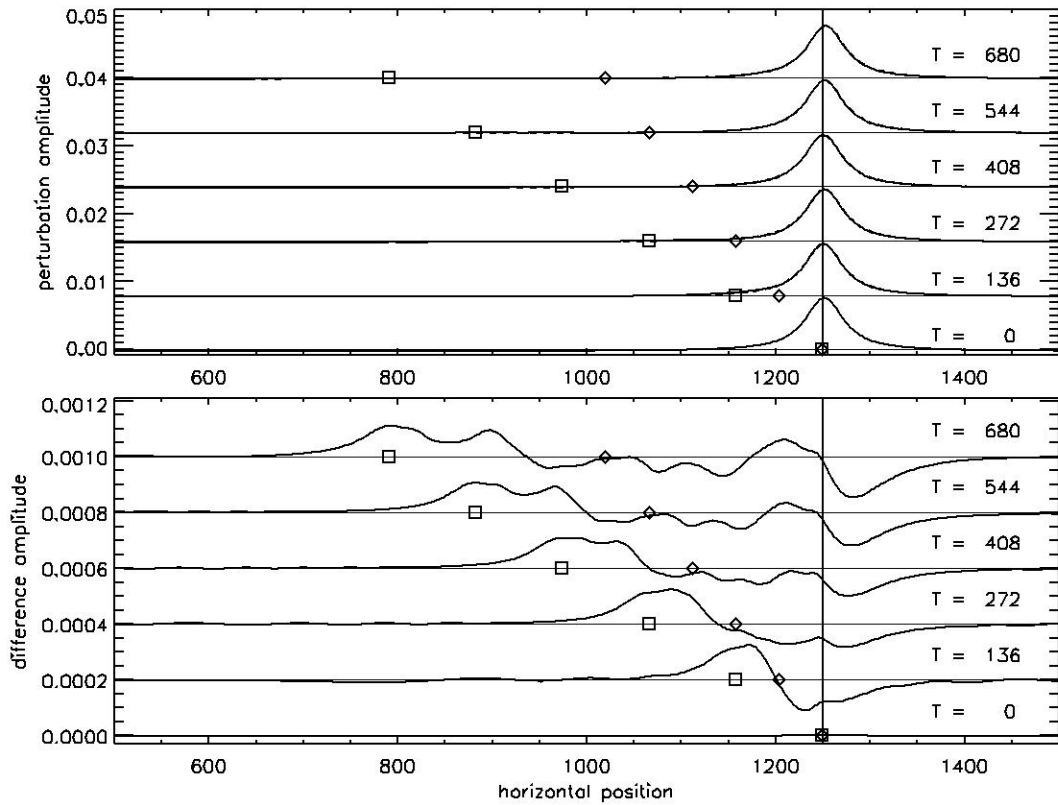
1053 **Figure 14:** Plots of crest creation timescales (t_c) for a sinusoidal perturbation as a
 1054 function of inverse amplitude (upper plot, asterisks) and wavelength (lower plot, crosses).
 1055 The solid lines between the data points are drawn for illustration and highlight both the
 1056 linear relationship between $1/\eta_0$ and t_c and the linear relationship between λ and t_c .

1057 **Figures**



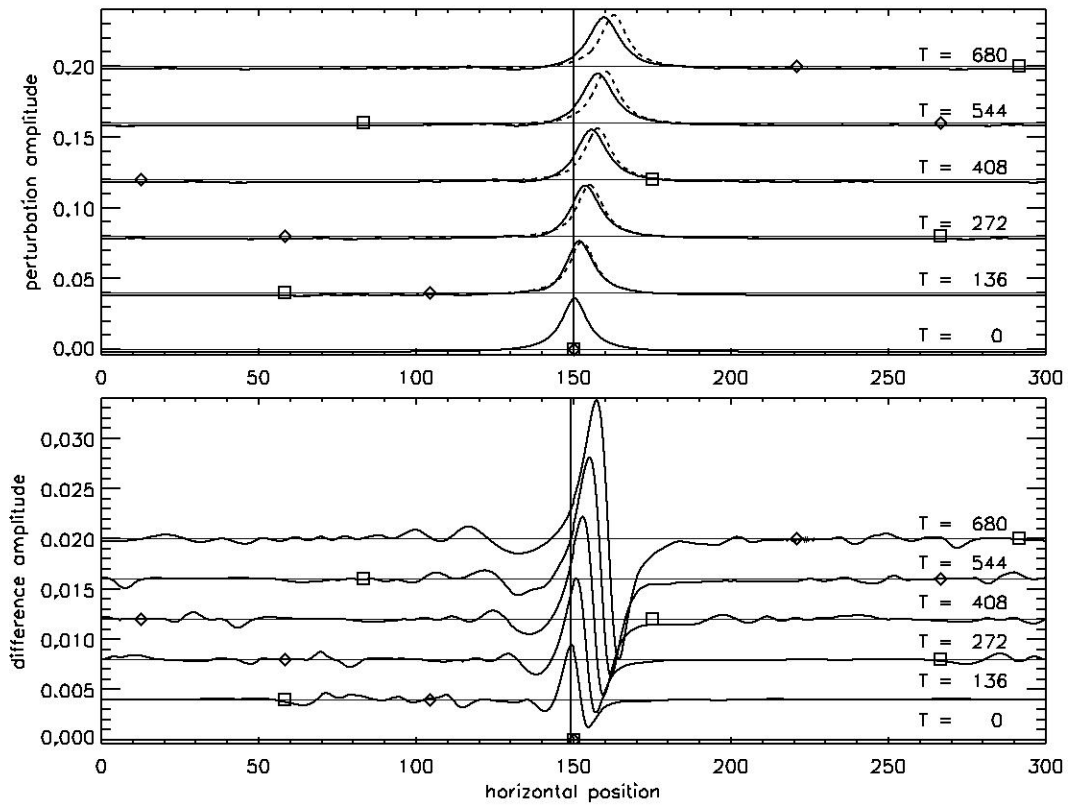
1058

1059 **Figure 1:** Panels (a) and (b): Density profiles considered by the BDO equation. Panel
 1060 (c): Raised cosine stability profile used in our models. The dashed lines of panel (c)
 1061 mark the FWHM of the cosine duct from $-h/2$ to $h/2$. Panel (d): Modal function for the
 1062 cosine stability profile computed for $z \geq 0$ (solid line) and anti-symmetrically reflected to
 1063 the region $z < 0$ (dashed line).



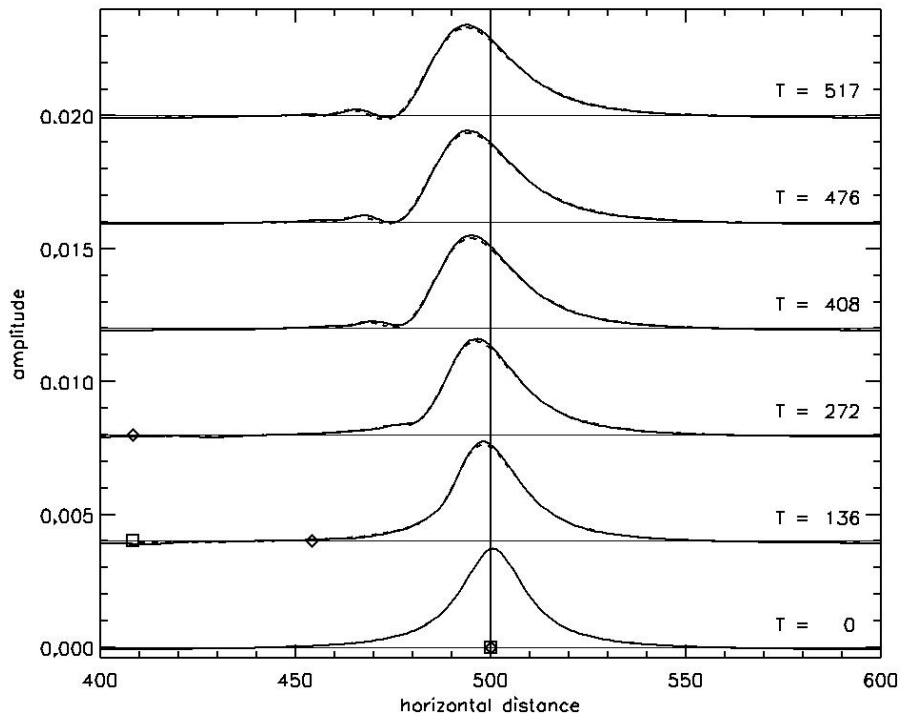
1064

1065 **Figure 2:** Time evolution of a $\lambda = 4\delta/\alpha\eta_0 = 25$ soliton depicted in a reference frame
 1066 moving with the long wave phase speed $c_0 = 0.33715$. The upper panel displays the
 1067 horizontally averaged potential temperature predicted by the NS (solid trace) and BDO
 1068 (dashed trace) equations. The lower panel plots the difference between the NS and BDO
 1069 solutions (NS minus BDO). The diamond moves leftward with velocity c_0 and represents
 1070 the origin in the stationary frame. The square moves leftward with velocity $-2c_0$
 1071 represents the point moving leftward with the long wave phase speed in the stationary
 1072 frame.



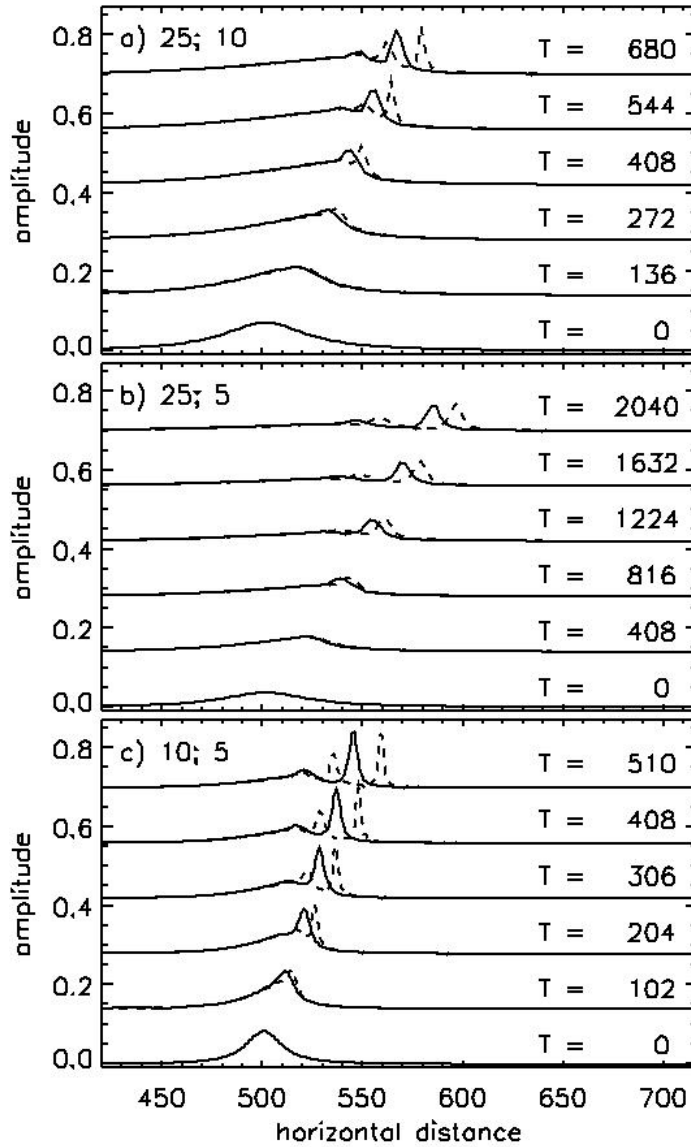
1073

1074 **Figure 3:** Time evolution of a $\lambda = 5$ soliton depicted in a reference frame moving with
 1075 the long wave phase speed $c_0 = 0.33715$. Panel (a) displays the horizontally averaged
 1076 potential temperature predicted by the NS (solid trace) and BDO (dashed trace)
 1077 equations. Panel (b) plots the difference between the NS and BDO solutions (NS minus
 1078 BDO).



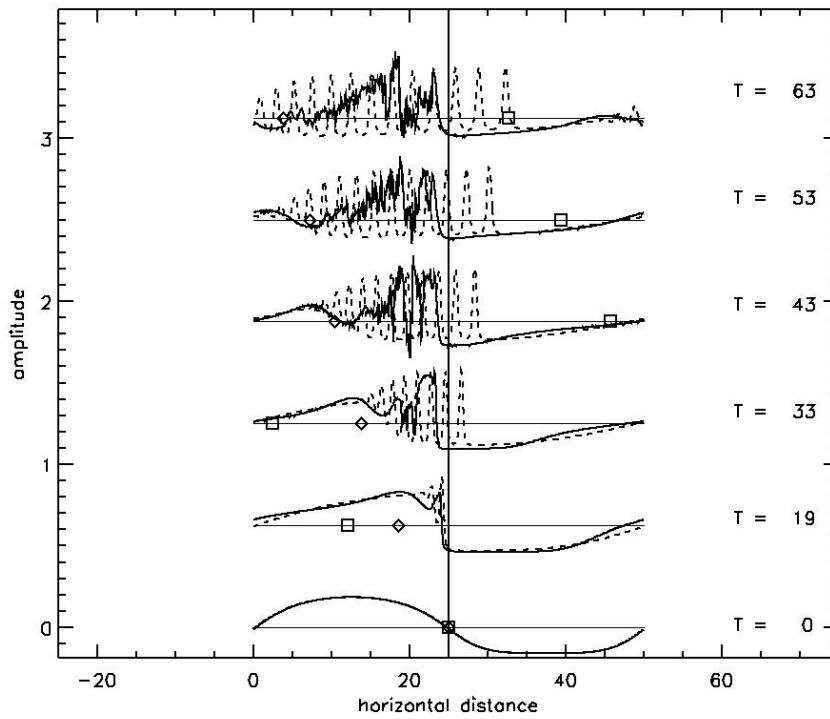
1079

1080 **Figure 4:** Time evolution of a $\lambda = 10$, $S = 0.2$ perturbation shown in a reference frame
 1081 moving with the long-wave phase speed $c_0 = 0.33715$. Displayed are the horizontally
 1082 averaged potential temperature predicted by the NS (solid trace) and BDO (dashed trace)
 1083 equations.



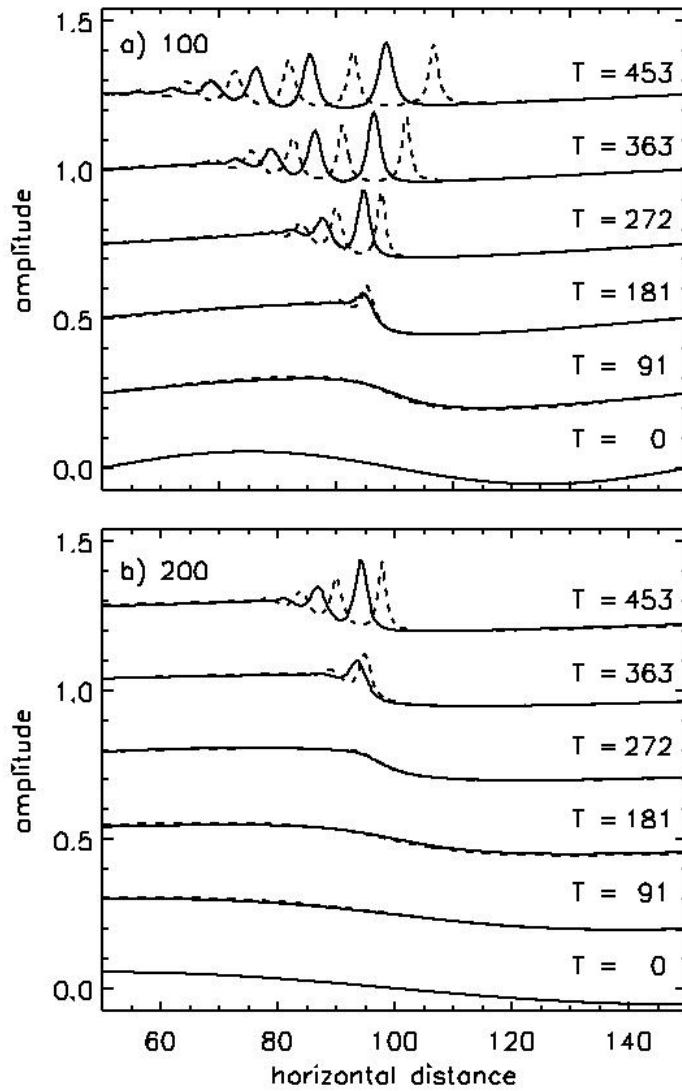
1084

1085 **Figure 5:** Time evolution of three soliton-like initial conditions defined by Eq. 16. Non-
 1086 dimensional times are listed above each trace. Panel a) shows the results of a $\lambda = 25$, $S =$
 1087 10 perturbation. Panel b) shows the results of a $\lambda = 25$, $S = 5$ perturbation. Panel c)
 1088 shows the results of a $\lambda = 10$, $S = 5$ perturbation. Displayed are the horizontally-
 1089 averaged potential temperature predicted by the NS (solid trace) and BDO (dashed trace)
 1090 equations.



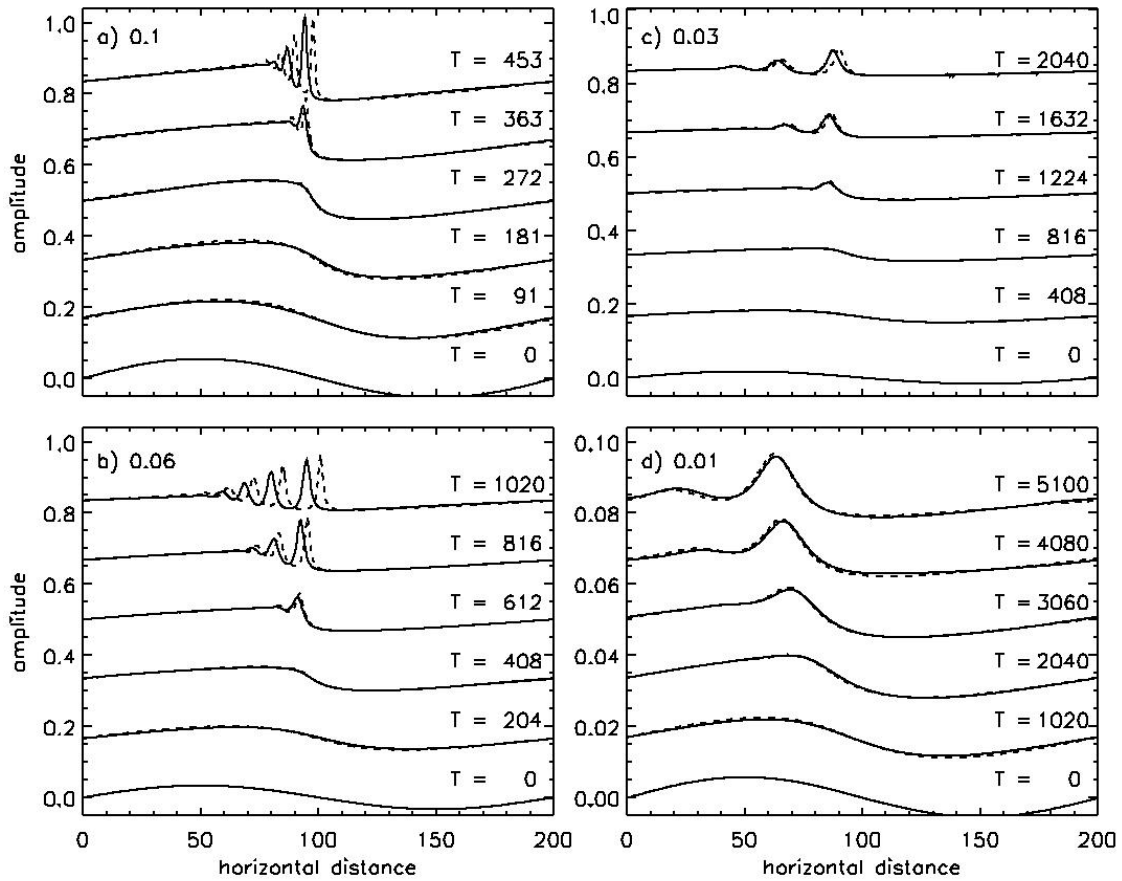
1091

1092 **Figure 6:** Time evolution of a $\lambda = 50$ $\eta_0 = 0.5$ sinusoidal perturbation. The solid line is
 1093 the NS solution and the dashed line is the BDO solution.



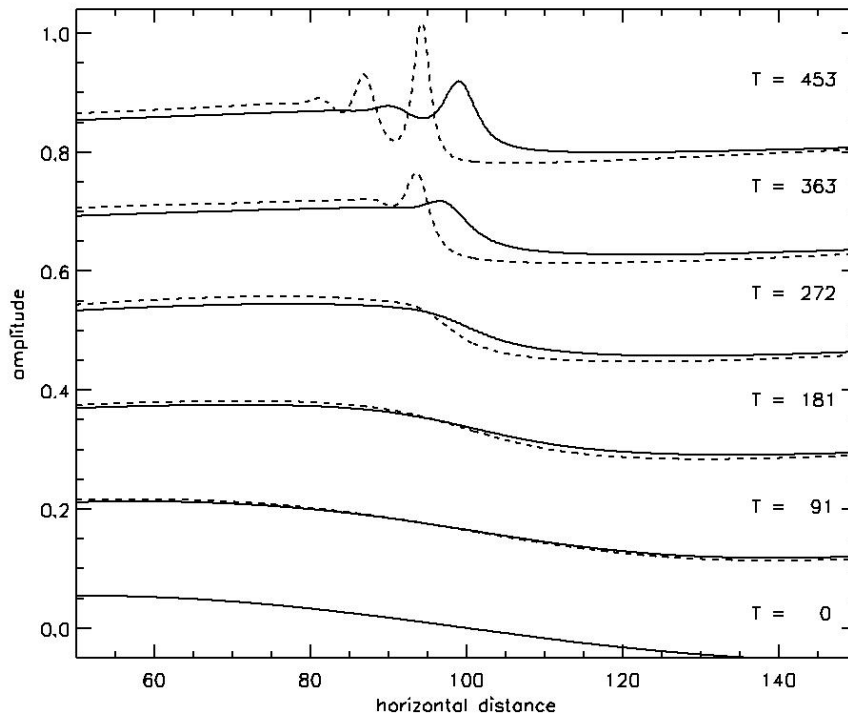
1094

1095 **Figure 7:** Panel a) time evolution of a $\lambda = 100$ $\eta_0 = 0.1$ sinusoidal perturbation. Panel b)
 1096 time evolution of a $\lambda = 200$ $\eta_0 = 0.1$ sinusoidal perturbation. The solid line is the NS
 1097 solution and the dashed line is the BDO solution. Both horizontal and amplitude scales
 1098 are the same (only half of the $\lambda = 200$ wave in panel b) is shown).



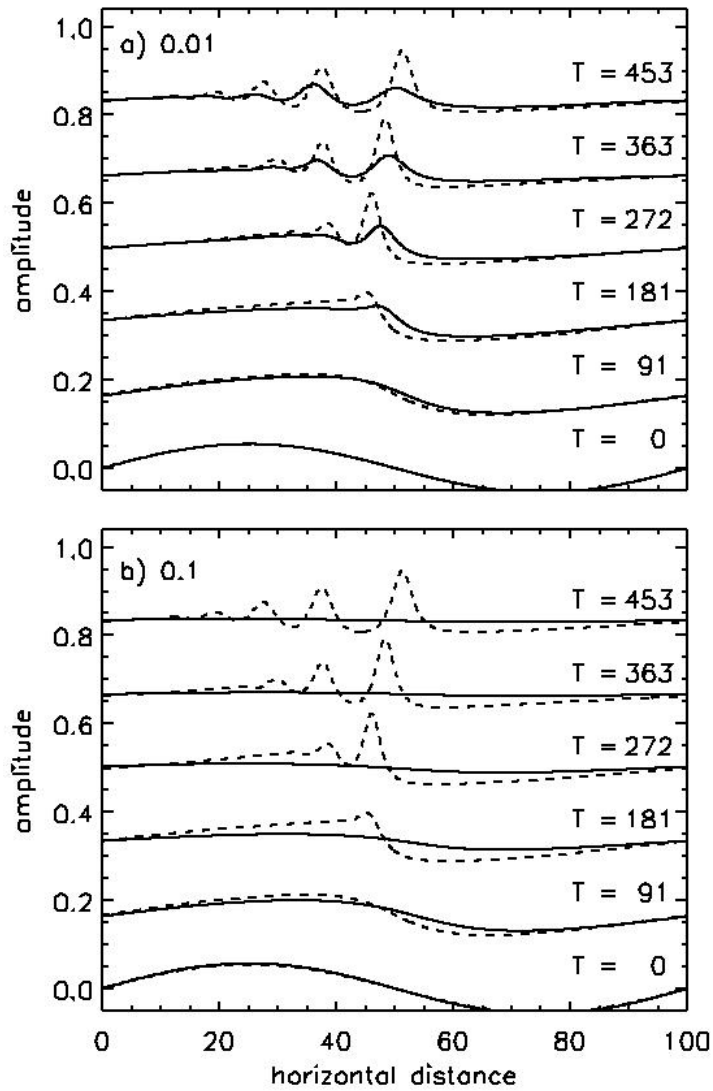
1099

1100 **Figure 8:** Time evolution of a $\lambda = 200$ perturbation with amplitude a) $\eta_0 = 0.1$, b) $\eta_0 =$
 1101 0.06 , c) $\eta_0 = 0.03$, and d) $\eta_0 = 0.01$. Note that the scale of panel d) is a factor of 10
 1102 smaller than panels a), b), and c). The solid line is the NS solution and the dashed line is
 1103 the BDO solution.



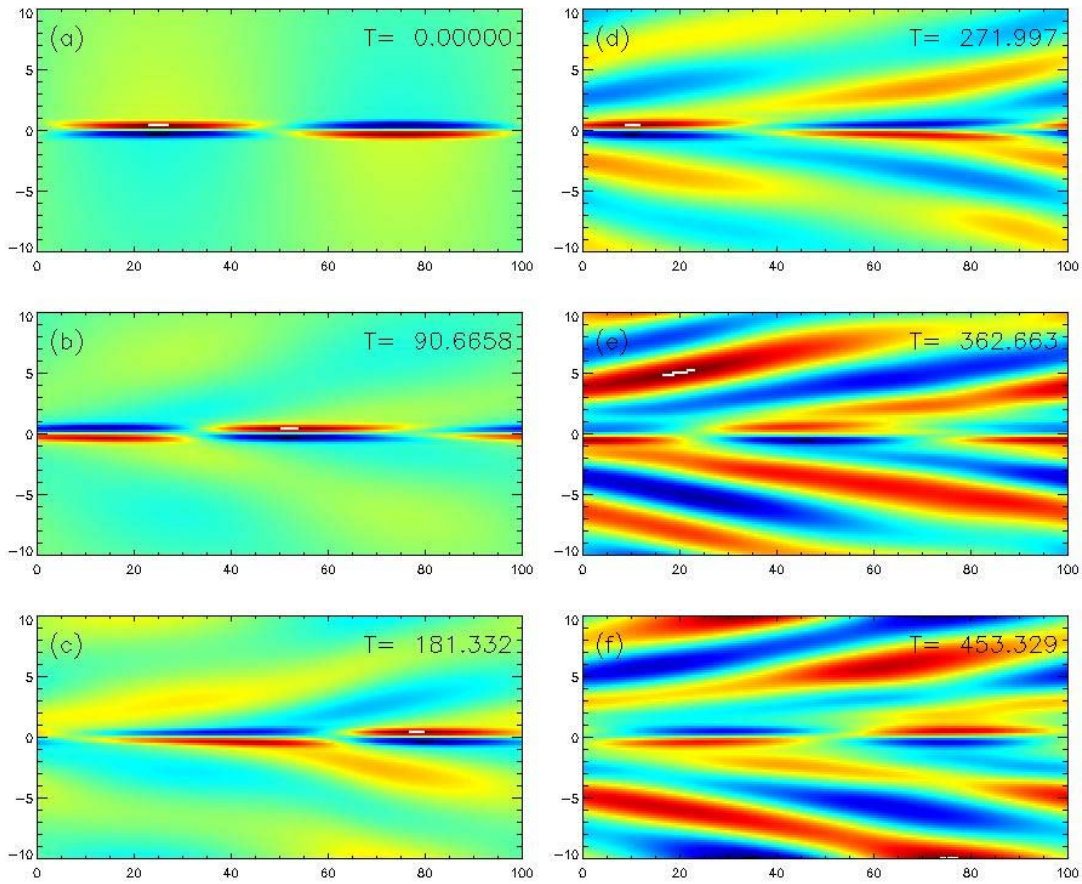
1104

1105 **Figure 9:** Time evolution of a $\lambda = 200$ $\eta_0 = 0.1$ sinusoidal perturbation in the presence of
 1106 viscosity. The solid line is the NS solution with a Reynolds number = 13090.0 ($\nu = 100$
 1107 m^2s^{-1}) and the dashed line is the NS solution in the absence of viscosity ($\text{Re} =$
 1108 1.309×10^{10}).



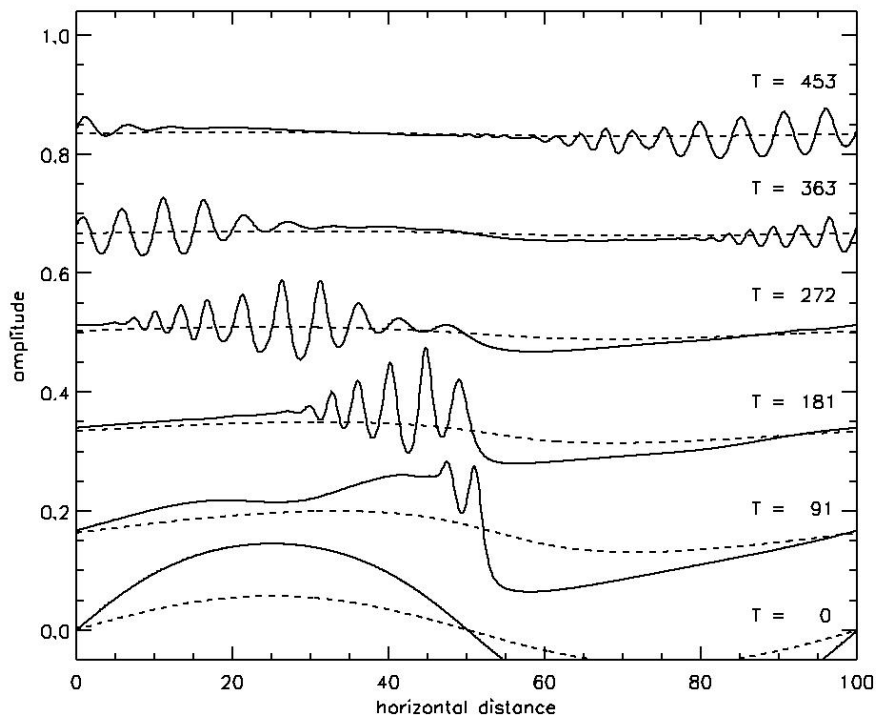
1109

1110 **Figure 10:** Evolution of a $\lambda = 100$ $\eta_0 = 0.1$ sine wave perturbation in the presence of a
 1111 non-zero background stability (solid line) and in the presence of a strictly neutral
 1112 background (dashed line). The background stability in panel a) is $N_B^2 = 0.01$ and the
 1113 stability in panel b) is $N_B^2 = 0.1$.



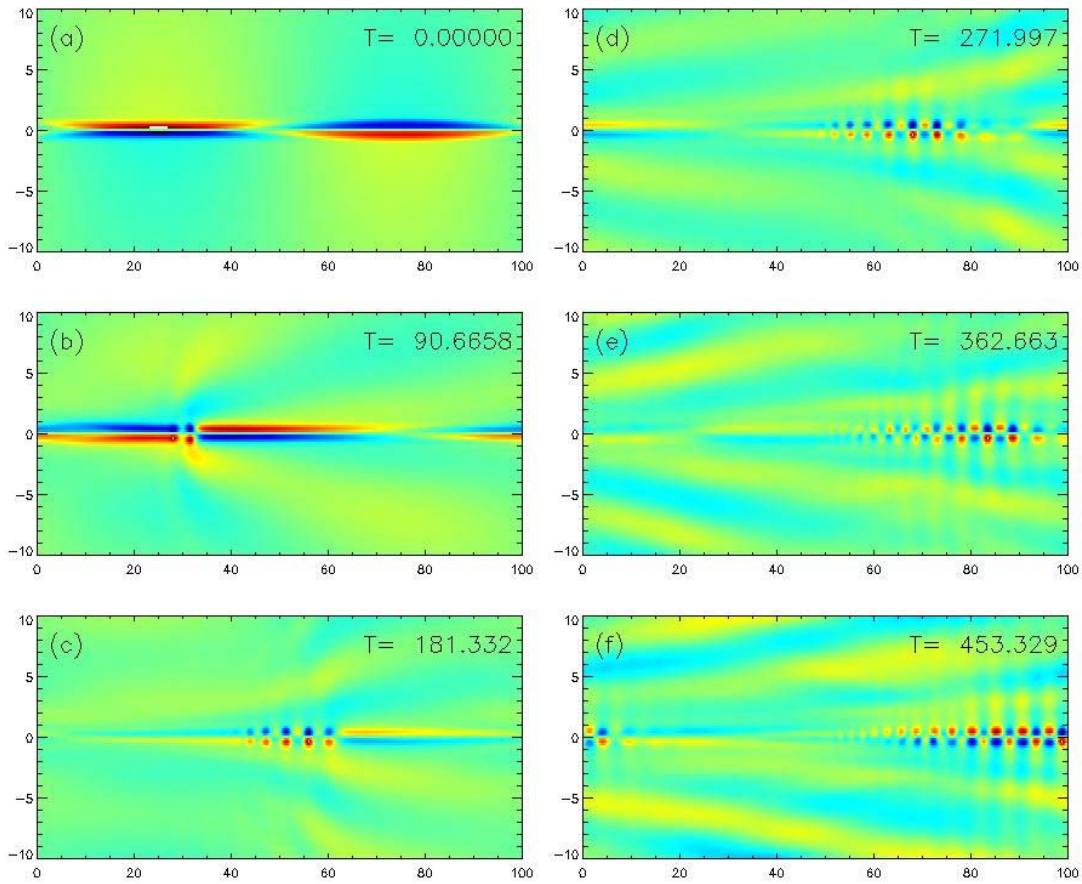
1114

1115 **Figure 11:** Evolution of a $\lambda = 100$ $\eta_0 = 0.1$ sine wave perturbation in the presence of a
 1116 non-zero background stability $N_B^2 = 0.1$. Displayed is the false colored perturbation
 1117 potential temperature field at six different times. Blue represents colder denser fluid
 1118 while red represents warmer less dense fluid.



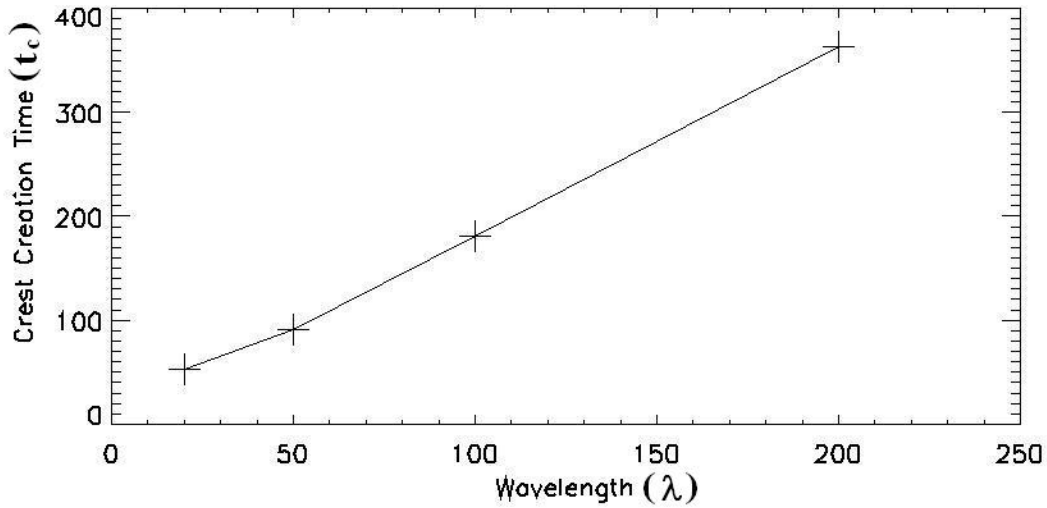
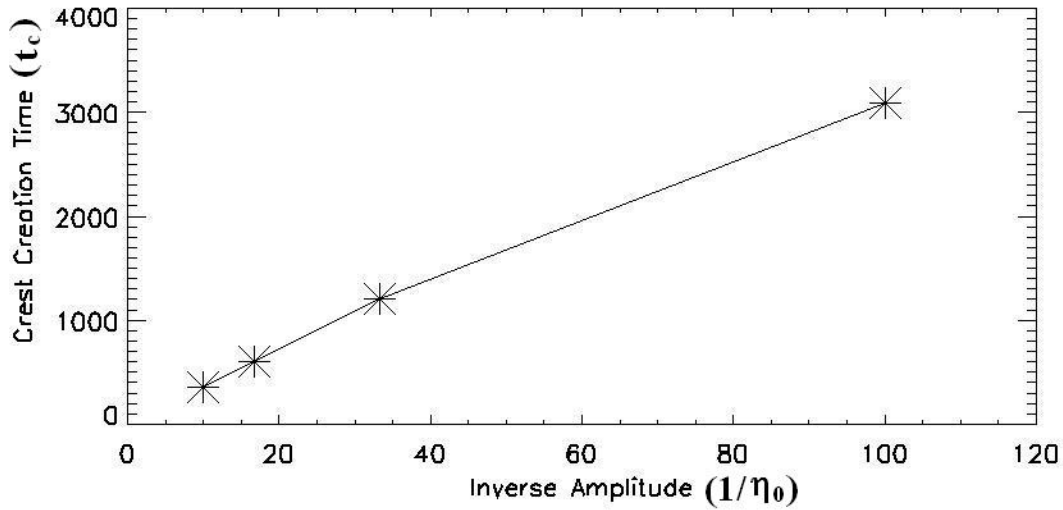
1119

1120 **Figure 12:** Evolution of a $\lambda = 100$ $\eta_0 = 0.3$ sine wave perturbation (solid line) and a $\lambda =$
 1121 100 $\eta_0 = 0.1$ sine wave perturbation (dashed line) in the presence of a non-zero
 1122 background stability $N_B^2 = 0.1$.



1123

1124 **Figure 13:** Evolution of a $\lambda = 100$ $\eta_0 = 0.3$ sine wave perturbation in the presence of a
 1125 non-zero background stability $N_B^2 = 0.1$. Displayed is the false colored perturbation
 1126 potential temperature field at six different times. Blue represents colder denser fluid
 1127 while red represents warmer less dense fluid.



1128

1129 **Figure 14:** Plots of crest creation timescales (t_c) for a sinusoidal perturbation as a
 1130 function of inverse amplitude (upper plot, asterisks) and wavelength (lower plot, crosses).

1131 The solid lines between the data points are drawn for illustration and highlight both the

1132 inverse relationship between $1/\eta_0$ and t_c and the linear relationship between λ and t_c .

1133